Modelling of Grain Boundary Segregation for Nanocrystalline alloys

Applied to Pd-based Alloys

by Xiaoyezi Liu

4582527

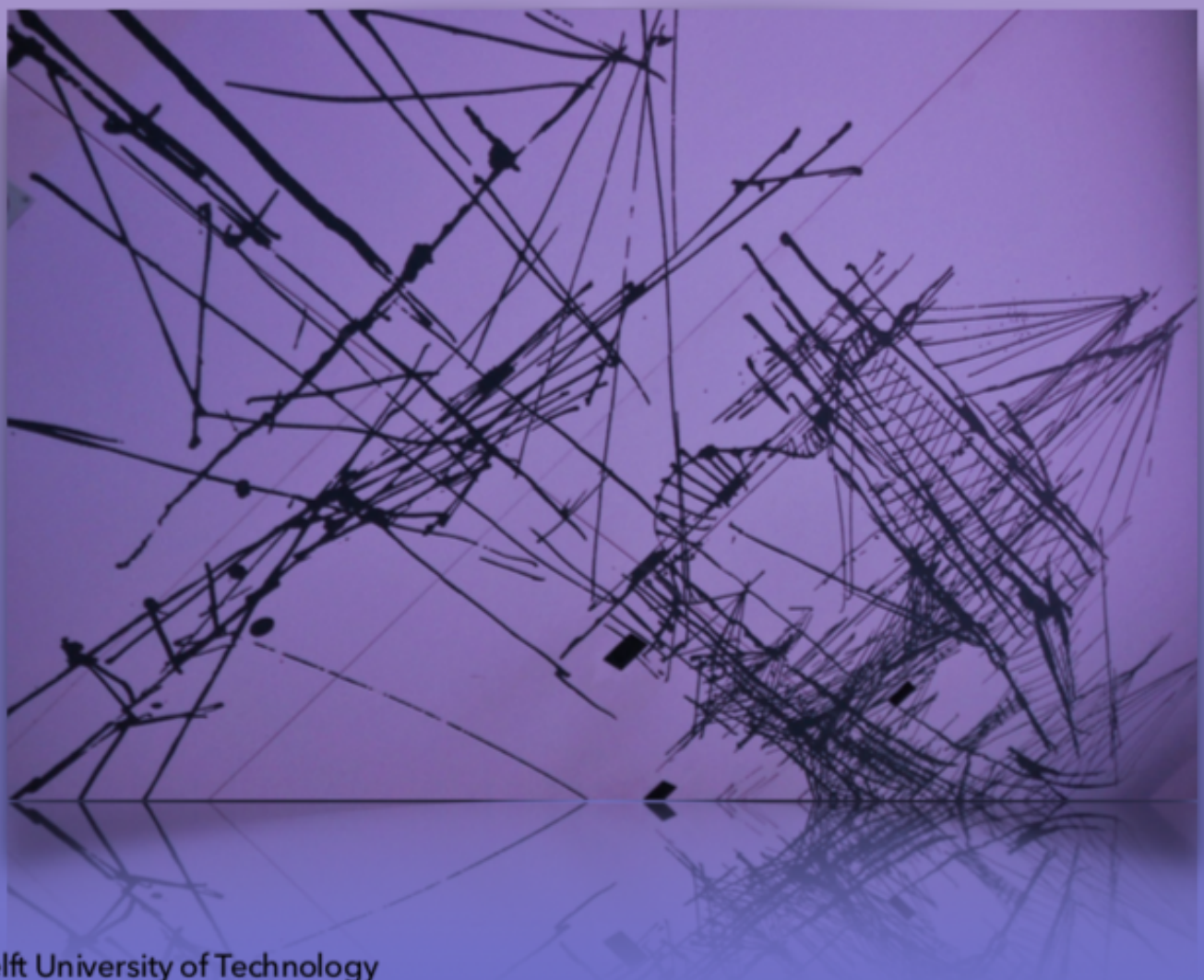

Delft University of Technology

Modelling of Grain Boundary Segregation for Nanocrystalline Alloys—Applied to Pd-based Alloys

Author:
Xiaoyezi LIU
4582527

Supervisor:
Amarante BOTTGER
Meng ZHAO

Thesis Committee:
Dr.A.J.Bottger
Dr.W.G.Sloof
Dr.M.H.F.Sluiter
Exile Member:
Dr.M.Zhao

Master of Science thesis submitted in fulfillment of the requirements for the degree of Msc Material Science and engineering

of

Delft university of Technology
Mechanical, Maritime and Materials Engineering Faculty

Abstract

The Pd-based metal membranes have been focused on many studies, because they are the most promising candidates for hydrogen separation. If Pd-based membranes are designed in nanoscale, then the introduced high volume fraction of grain boundaries can act as fast diffusion paths for hydrogen atoms that leading to an increase of hydrogen separation rate. However, due to the substantial amounts of grain boundaries, the nanocrystalline material tends to show a rapid grain growth at operating temperature (that leading to the coarse grains), which may lead to the failure of this membrane in further applications. However, grain growth could be effectively inhibited by thermodynamic stabilization method–that is solute segregation to grain boundary region. In this thesis, a thermodynamic grain boundary segregation model is developed and is applied to many types of metallic binary alloys, including the Pd-Cu, Pd-Zr, Pd-Y, Fe-Zr, Y-Fe and so on. From this model, the segregation tendency of alloying constituents is determined, and the solute concentration in grain boundary is obtained. Moreover, the grain boundary energy (GB) of investigated alloys can be calculated via this model, by comparing the calculated GB energy with that of pure Pd, we are able to determine whether these alloys can be stabilized by the segregation-introduced thermodynamic stabilization. These calculated results have been compared with those reported in the literature, verifying the predictability of this model. In addition, X-ray diffraction (XRD) analysis including the XRD residual stress measurement and X-ray peak broadening analysis have been performed on both $Pd_{0.7}Cu_{0.3}$ and pure Pd thin films, the experimental results will help us determine whether the solute segregation occurs and whether this alloy can be stabilized by the solute segregation.

Acknowledgements

I would like to express my gratefulness to Dr.Amarante Bottger, a respectable and responsible scholar, who has provided me with valuable guidance and creative ideas in every stage of the thesis project, and has provided me with useful instructions in writing the thesis.

I shall extend my thanks to my another supervisor Meng zhao for his kindness and help, who also has provided me with valuable guidance in this thesis project, and has helped me to develop the fundamental and essential academic competence.

Without their enlightening instructions, impressive kindness and patience, I could not have completed my thesis.

I'd like to thank my family, friends, who have been always standing by me and giving me the courage and infinite support to continue forward. Last I'd like to thank the student life in Netherlands, which has taught me to be a independent person and to better understand myself that knowing what is important in my life, and to learn to be calm and look at problems dialectically. A good mentality is very important no matter what we do.

Contents

List of Figures

List of Tables

List of Symbols

GB	grain boundary region	
c_0	initial solute concentration of bulk or GB region before GB segregation	
c_1	solute concentration of bulk region after GB segregation	
c_2	solute concentration of GB region after GB segregation	
D	grain size	nm
t	grain boundary thickness	nm
f_{bulk}	volume fraction of bulk region	
f_{gb}	volume fraction of gb	
G_{bulk}	free energy of bulk region	kJ/mol
G_{gb}	free energy of GB region	kJ/mol
γ	free energy of interfacial area	kJ/m^2
ΔH_{size}	size mismatch energy between solute and solvent atoms	kJ/mol
H^{form}	the formation enthalpy	kJ/mol
H^{fuse}	the fuse enthalpy	kJ/mol
f_B^A	the degree of A surrouded by B	
T	temperature	K
S_c	ASD factor	
del	the fraction of amorphous phase in GB region	
S	entropy of mixing	kJ/mol
g	an introduced constant	
m	an introduced parameter (estimate the chemical short-range order)	
Γ	solute excess	mol/m^2
γ_{gb}	the GB energy of a certain alloy	mJ/m^2

Chapter 1

Introduction

Currently, the global society still highly depends on fossil fuels, i.e., primarily coal, fuel oil or natural gas. These resources have been used to power automobiles, plants, factories and to support our daily life, leading to the accumulation of greenhouse gases. Because of the large emissions of the greenhouse gases, we are facing the accelerated global warming [1], which may result in many side effects, i.e., the increased desertification, water shortage, starvation, malnutrition, and increased deaths due to the shortages of food and crops. Nevertheless, the hydrogen-based economy can potentially provide a promote approach to tackle the global warming effects while maintaining our standard of living [1]. The reason behind is that hydrogen is considered as an ideal energy carrier and can be used as a fuel to power many devices, which is environmental-friendly and competitive to conventional fossil fuels with a lower cost. In principle, hydrogen can be directly produced from water by supplying an extra renewable energy resource, such as the solar, wind or nuclear, and the whole process only generates less detrimental environment effects [2].

Hydrogen can be produced in several various ways including electrolysis of water, gasification of coal, steam reforming or partial oxidation of natural gas [3]. However, hydrogen gas is likely to mix with other gases (i.e., O_2, CO, CO_2, steam, N_2 and H_2S) as the end-product. Therefore, in order to obtain high-purity hydrogen gases, an additional purification is needed, and the generated H_2 could be utilized as a fuel for low temperature polymers or alkaline electrolyte fuel cells. In order to separate and then purify the hydrogen from other gases, membrane technology is introduced. This technology serves as an effective method due to its low operating costs and low energy consumption [4], and the function of dense membrane is to dissociate the absorbed molecular H_2 on its surface then to separate H_2 into single H atomic form. Later, the high diffusivity of hydrogen atom can penetrate the membrane and recombine into the molecular on the other side of the membrane and then diffuse away. The complete procedure of diffusion of hydrogen atom permits the highly selective separation H_2 from other gas mixtures. Therefore, the properties of membrane are very important. Normally, palladium metal membranes are the most promising candidates for hydrogen separation, due to a higher solubility of hydrogen in bulk region over a wide temperature range [3]. And a report shows 99.9 % of high purity hydrogen can be directly obtained from the palladium based membrane tube incorporated in steam reforming reactor[5].

However, there are some limitations of pure palladium membrane. The α to β phase transition that attributed to the absorption of H atoms, which can lead to the changes in lattice parameters of Pd, thus giving rise to the strain and recrystallization [6]. This phase transition is detrimental to the effectively of Pd. Other limitations include the instability at high temperature, poisoning and high cost. The metallic nature of

Pd gives rise to interactions with sulfur presented in environments, which may generate contaminations at the surface of Pd membranes and influence the dissociation of adsorbed H_2 [7]. Alloying pure Pd with other metallic elements, i.e., Ag, Zr, Cu, Ni and Y may relieve some of these problems. Some studies show the permeability of hydrogen in Pd-based alloys, i.e, Cu, Ag, Au, Y and Ce, was much higher than that of pure Pd, this is because hydrogen atoms have a higher solubility or higher diffusivity in these alloys. It has been reported that Pd-Cu is the most promising alloys in terms of permeability and sulfur resistance.[7]

If Pd-based membranes are designed in nanoscale, alloying also has the potential to suppress the instabilities of these pure nanocrystalline metals, especially being effective at high temperature. Also, the nanostructured Pd-based membranes may give rise to substantial grain boundaries, and these elements could act as fast diffusion pathways for hydrogen atoms, under certain condition, the diffusivity of H atoms can be 10 times higher than that of conventional Pd [2][8]. Moreover, the α to β phase transition that lead to the film delamination, can be effectively inhibited in some of Pd-based alloys, i.e., Pd-Fe [9], Pd-Pt [10], thus extending the thin film's service life. However, the nanostructured membranes still suffer from several limitations: When the crystallite size of polycrystalline material is reduced to the nanoscale, a high volume fraction of grain boundaries can be introduced, which have an associated energy penalty and may lead to a rapid grain growth at the operating temperature [11], and the coarsening tendency may restrict the usages of these membranes in further applications. Nevertheless, if nanostructured stability is enhanced, these materials could be used more broadly with a longer product service life.

In order to inhibit or decrease the grain growth of nanocrystalline materials, two mechanisms have been formed, including kinetic stabilization and thermodynamic stabilization. Kinetic stabilization is involved in stopping the grain growth by pinning, which can be achieved by using a second-phase particle (Zenner pinning), solute drag or pore[12]. However, the pinning procedure only has limited effects, especially at high temperature, because the mobility of grain boundaries can be thermally activated, and thus pinning force could be overcome at high temperature that leading to a grain growth. Whereas, the thermodynamic stabilization mechanism has a weaker temperature dependence and is independent of time, thus it is more effective in impeding the grain growths at high temperature, if no precipitates are formed. The thermodynamic approach involves in lowering the Gibbs free energy of the alloy system by solute segregation to grain boundary region. The specific principle of thermodynamic stabilization will be briefly discussed in the later chapter.

The thesis is divided into three parts, the first part will explain the procedure for developing the thermodynamic grain boundary segregation model, aiming at predicting the segregation tendency and the grain size stability of nanocrystalline alloy. The second part will explain the modelling results of the different metallic binary alloys. These calculated results will be compared with those reported in the literature, which can verify the feasibility and predictability of this GB segregation model. Moreover, in this part, the parameter discussions will also be displayed. Meanwhile, the theoretical results should be approved by the experimental investigations. Thus, in the third part of the thesis, X-ray diffraction measurements that performed on both the Pd-Cu and pure Pd thin films will be displayed. The experimental results will be compared to these generated from the theoretical model, the results will prove the feasibility and predictability of the GB segregation model.

Chapter 2

Grain boundary segregation and prior segregation models

2.1 Grain boundary segregation

Grain boundaries (GB) can contribute an extra energy term in the Gibbs free energy of the binary alloy system. A system that consisting of a large surface to volume ratio of grain boundaries tends to be unstable and is likely to reduce this energy in various ways, including the grain growth phenomenon, and the interactions between GB and other crystal defects. If grain boundaries interact with the point defeact (impurity atoms), then an localized accumulation of foreign atoms (alloying elements) at GB can occur, this process is called grain boundary segregation [13].

Grain boundary segregation can be divided into two types: non-equilibrium and equilibrium segregation [13]. Non-equilibrium grain boundary segregation involves interactions between solute atoms and excess vacancies. When vacancies diffuse into the grain boundaries, solute atoms prefer to settle down at this region, due to the existence of dragging forces between the vacancy-solute pairs. This phenomenon is more common in certain metallurgical operations such as quenching and irradiation. The other grain boundary segregation is associated with the local redistribution of solute atoms, where alloying atoms prefer to occupy grain boundary sites than those in bulk interiors to relieve the GB energy penalty. In this thesis, only equilibrium grain boundary segregation will be considered.

Before discussing the GB segregation models, initially, we will introduce some relevant theories behind them, which can serve as a guideline for the development of thermodynamic models. The theory of equilibrium solute segregation at grain boundary can be approached by analogy to the classical surface/gas adsorption isotherm theory. The only difference lies in the fact that for the surface adsorption, adsorbed atoms coexist with vacant sites, whereas for GB segregation, segregated atoms are mixed with solvent atoms. In 1918, Langmuir raised a segregation theory called Langmuir (monolayer) type adsorption, which is obeyed by some solid adsorbent/gaseous adsorbate systems. Meanwhile, according to this theory, the total number of adsorbing sites is fixed, and the occupation of each site does not influence the occupation of its neighbouring sites[14]. Later, McLean took a further step to establish a equilibrium solute segregation theory by analogy to Langmuir solid/gas adsorption. According to the McLean's equation, segregation develops with the increase of solute concentration and with the reduction of temperature, however the difficulty of employing this equation lies in the estimation of differential segregation free energy [14]. Therefore, in order to overcome this difficulty, Brunauer, Deming and Teller raised a multilayer adsorption isotherm theory by analogy to Langmuir

type surface adsorption isotherm, and the grain boundary analogue form of this theory can be derived, where the solute segregation can build up to several monatomic layers in stead of the saturation coverage or the Langmuir type. So far, all the theories described above ignore the interactions between adjacent sites, however, it is not a valid assumption in practical applications, therefore, the Fowler-Guggenheim theory was developed, which takes into account the more complex interactions between neighboring atoms.

2.2 Grain boundary segregation models

Based on the theories mentioned above, several models were derived to predict the tendency of solute segregation of binary metal pairs, which include the Hondors and Seah, McLean, Defay, Wynblatt and Ku, and Darling et al. and so on [15].

Honduras and Sean model made a rough estimation for the segregation enthalpy of impurities in steel, where the enthalpy was directly related to the solubility of bulk of this alloy system, without involving any energy of grain boundaries, moreover, this model is empirical that strongly relying on experimental segregation data, thus it is restricted to a small range of binary alloys. McLean model considered the elastic energy was the main driving force for solute segregation to grain boundary, and the purpose of grain boundary segregation was to eliminate the elastic strain energy between solute and solvent atoms. He suggested to use the Eshelby-type continuum linear elastic approach to evaluate the segregation energy. However, based on this method, the calculated segregation energy term is always positive, which will predict a solute segregation to grain boundary for all the different alloying systems. Wynblatt-Ku model was developed for predicting the surface segregation enthalpy of binary alloys. Darling et al. suggested to introduce a parameter to account for the distinction between surface and grain boundary, after proper modifications, the surface segregation model is also applicable to grain boundary segregation. As for Defay segregation model, segregation enthalpy only contains the chemical contributions without including other energy terms.

However, most of the models discussed above are mainly designed for predicting the free surface segregation, or they are lack of some important parameters that reflecting the properties of grain boundaries. Therefore, new models should be developed to describe the grain boundary segregation.

Trelewicz and Schuh (TS) suggested a regular solution model to predict the stability of general non-dilute nanostructured binary alloys by GB segregation. The basic idea of this model is to calculate the change of total Gibbs energy of polycrystal upon alloying, and a metastable equilibrium grain size may exist in alloy systems due to the solute segregation to GBs. In TS model, the full volume system of a binary alloy is divided into three parts: bulk region, GB region and an interface area (that separating the bulk and GB regions), where both bulk and GB regions are considered as solid solutions, and there are many bond pairs crossing the interface and connecting these two regions. Based on this model, for an arbitrary alloy system, the total Gibbs free energy ΔG is formulated by the separated contributions from enthalpy of mixing and entropy of mixing, where the free energy of mixing can be evaluated by the

summation of nearest-neighbor interaction energies of all bond pairs, which individually distribute within bulk, GB and interface these three regions. Whereas, the total entropy of mixing can be estimated by using statistical configuration entropy. Later, the equilibrium state of this binary alloy can be determined by minimizing the total Gibbs free energy ΔG, with the simultaneous variations in global solute concentration and in volume fraction of GB region. However, there are some limitations of this model. For example, elastic size mismatch strain energy is not taken into account, whereas in some alloying systems, the size-misfit elastic energy is very large and is considered as the main driving force for solute segregation to grain boundaries, i.e., in Fe-Zr, solutes Zr in solvents Fe have a atomic size difference +28%, the obtained segregation enthalpy $H_{seg} = -92$ kJ/mol, is numerically equal to the elastic strain energy between Fe and Zr atoms [12][16]. Moreover, grain boundary region is considered as a solid solution in TS model. Nevertheless, amorphous phase could be formed via interdiffusion at the interface of certain types of alloy systems, i.e., Ni-Ti, Ni-Zr, Cu-Y and Ti-Si [4]. Therefore, it is also reasonable to assume the GB region as a partial amorphous phase and a partial solid solution. Furthermore, some addition energy terms (such as fusion enthalpy) that describing the atomic disorder (amorphization) at GB region should be incorporated.

In this thesis, we will formulate a improved thermodynamic grain boundary segregation model based on the concept of the TS model, to predict the segregation behavior and the thermodynamic stability (grain growth) of nanocrystalline binary Pd-based alloys in a more reasonable way. In our grain boundary segregation model, the shape of a nanocrystalline binary alloy system will be initially defined. Then, energy terms that contributed from different regions of the alloy system will be discussed separately. The individual mixing enthalpies of bulk and grain boundary regions will be formulated by using Miedema model, rather than by taking the product of the number of bond pairs distributed within certain region and its corresponding bond energies [17]. Compared with TS model, the modified model could be not only applicable to the case if grain boundary region is considered as a solid solution, but also applicable to the case if grain boundary region is considered as an amorphous phase. The entropy of mixing will be estimated by using statistical mechanics. We define the interface as an area that separating the bulk and grain boundary regions. The interfacial energy can be associated with the energy increase that stems from various bond pairs that bridge the two distinct regions. Moreover, some additional energy terms, i.e., the elastic strain, fusion enthalpy, will be added to establish a more reasonable model. In conclusion, the modified grain boundary segregation model is not only applicable for these alloys that show strong segregation tendencies, but also for those that exhibit weak segregation tendencies, and without limiting ourselves to a dilute limit. This model is able to provide some qualitative guidelines for understanding the thermodynamic behavior of various nanocrystalline binary alloys, however, if quantitative analysis is needed, more factors should be taken into account, i.e., the more complex forms of interactions and the competing phases.

Chapter 3

The modified grain boundary segregation model

3.1 Framework of modified grain boundary segregation model

The modified grain boundary segregation model can be utilized to predict segregation tendencies of various binary alloy systems. To derive this model, some assumptions should be made beforehand: (1) Nanocrystalline alloy system will be considered as a regular solution rather than assuming a dilute limit. Because the majority of experimental nanocrystalline alloys are non-dilute [19], in these alloy systems, solute atoms are uniformly mixed with solvent atoms rather than form a highly immiscible solution, therefore, appropriate models should be developed for these non-dilute alloys. (2) We neglect the formation of secondary or the intermetallic phase, and only consider a single phase, this is because extra phases may lead to additional thermodynamic potentials. (3) Only the nearest-neighbour pairwise interactions will be considered.

For a nanocrystalline binary alloy, it is assumed as a regular solution consisting of solute atoms A and solvent atoms B, the alloy composition can be expressed as A_cB_{1-c}, where c denotes the solute concentration, and $1-c$ denotes the solvent concentration. The full volume system of this binary alloy can be considered as as a cubic grain of size D, which is divided into a bulk region (FIGURE 3.1: blue colour) and a grain boundary region (FIGURE 3.1: yellow colour). An interface (FIGURE 3.1: dashed dark blue line) exists that connecting the two distinct regions. The shape of the alloy system is represented in following figure.

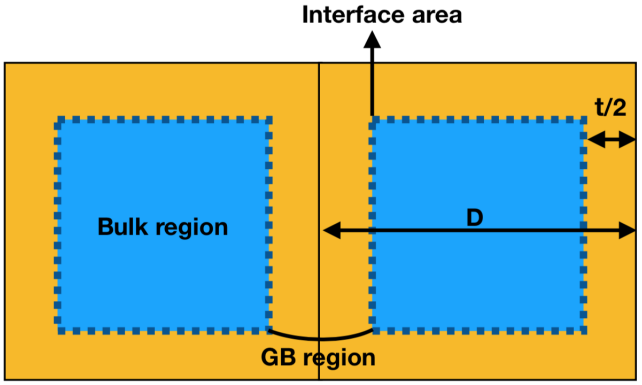

FIGURE 3.1: Two connected cube shape grains in 2D

Where, according to the figure, two identical cubic grains (size D) are connected with each other, each cube represents an alloying volume system. The outer cube represents a grain with size D, the inner cube represents the bulk region (blue colour), and the closed yellow region represents the grain boundary, with a finite grain boundary thickness $t/2$. Interface area is indicated by the dashed line. After defining the grain geometry, the volume fraction of bulk, f_{bulk}, and the volume fraction of grain boundary region, f_{gb} can be determined. The sum of f_{bulk} and f_{gb} satisfies 1.

$$f_{bulk} = (\frac{D-t}{D})^3 \tag{3.1}$$

$$f_{gb} = 1 - (\frac{D-t}{D})^3 \tag{3.2}$$

Where, the superscript 3 denotes the dimensionality of grain structure. And the numerical value 3 is not restricted to cubic structure, it also applicable for a general 3D polycrystal [17]. In addition, the volumetric atomic density can be normalized by correlating the total number of atoms with the volume fractions of individual region.

Before grain boundary segregation, we define the initial solute concentration as c_0, and the solute concentrations of bulk and GB regions are both equal to c_0, then alloy composition is expressed as $A_{c_0}B_{1-c_0}$. However, some alloying atoms prefer to occupy sites in grain boundary region rather than those in crystalline interiors, to minimize the total energy of the alloy system. Therefore, GB segregation occurs to relieve the energy penalty of interfaces. After segregation, the solute concentration of bulk changes into c_1, whereas the solute concentration of GB region becomes c_2. It is mentioned that c_0, c_1 and c_2 will obey the conservation law during the whole segregation procedure, and they can associate with each other by a volume fraction-weighted average. This is because we assume a closed binary alloy system, the total number of solute (A) atoms and solvent (B) atoms are fixed. The relation between c_0, c_1 and c_2 is given as

$$c_0 = f_{bulk}c_1 + f_{gb}c_2 \tag{3.3}$$

3.2 Free energy function

In our thermodynamic grain boundary segregation model, the total change of Gibbs free energy of the binary alloy system before and after segregation will be determined, which will be utilized to evaluate whether solute segregation can occur. For the cubic-shaped grain represented in figure 1, we define the total free energy of system consists of three parts: (1) the free energy of bulk region, G_{bulk}; (2) the free energy of grain boundary region, G_{gb}; (3) the free energy of interfacial area, γ. Therefore, the total free energy of the alloy system can be expressed as

$$G_{total} = G_{bulk} + G_{gb} + \gamma \tag{3.4}$$

Before grain boundary segregation, we define the total free energy of system as G^1_{total}, whereas, after segregation, the total free energy is assigned as G^2_{total}, therefore, the total change of free energy that attributed to solute segregation can be expressed as

$$\Delta G_{total} = G^2_{total} - G^1_{total} \tag{3.5}$$

If $\Delta G_{total} < 0$, solute segregation might occur, because solute atoms tend to diffuse into the grain boundary sites to lower the energy of system; while if $\Delta G_{total} > 0$,

solute segregation might not occur. In the following sections, the free energy of different regions will be explained separately.

3.3 The free energy of bulk

For the binary alloy system, A_cB_{1-c}, we consider the bulk region as a solid solution, where component A is randomly distributed over the atom sites of the other component B. Before segregation, solute concentration of bulk is c_0, and solvent concentration is $1 - c_0$. The free energy of bulk region (FIGURE 1.1) can be estimated by the energetic contributions from four parts: (1) the formation enthalpy of solid solution, H_{bulk}^{form}, which evaluates whether alloy compound will form at certain concentrations; (2) the random entropy of mixing, S_{bulk}; (3) the elastic mismatch strain energy, ΔH_{size}, which incorporates the difference of atomic volume between solute and solvent atoms; (4) The structure contribution, $\Delta H_{structure}$, which indicates the preference of transition metals to crystallize in one type of crystal structure (bcc, hcp and fcc) [18], also reflects the change of lattice stability of solid solution with respect to the different atomic concentration [19]. According to the literature [18], for binary alloys that consist of a noble metal (i.e., Cu) and an fcc or hcp transition metal, normally, the structural contribution $\Delta H_{structure}$ will be neglected, moreover, the structural term will be absent in amorphous alloy. Thus, before grain boundary segregation, the free energy of bulk region can be given as

$$G_{bulkc_0} = H_{bulkc_0}^{form} - TS_{bulkc_0} + \Delta H_{size} \tag{3.6}$$

After GB segregation, solute concentration of bulk will become c_1, and its corresponding alloy composition will be $Ac_1B_{1-c_1}$. Then, the free energy of bulk region can be expressed as

$$G_{bulkc_1} = H_{bulkc_1}^{form} - TS_{bulkc_1} + \Delta H_{size} \tag{3.7}$$

Where, in above equations, T denotes temperature. The mixing entropy terms S_{bulkc_0} and S_{bulkc_1} can be derived via utilizing the standard statistical approach, if we assume a random distribution of solute and solvent atoms.

3.3.1 Formation enthalpy of binary alloy

To calculate the formation enthalpy of the binary alloy, Miedema model will be applied. The semi-empirical theory was propounded by Miedema and his colleagues around 1970s, aiming at predicting the formation enthalpy and other basic properties of various alloys including the solid solution, amorphous alloy and intermetallic compounds [20]. The essence of Miedema model is to quantitatively evaluate the energy effects when two distinct components are brought into contact. Based on Miedema theory, the standard formation enthalpy can be mainly estimated by two important parameters the electronegativity difference and the electron-density discontinuity [20]. If pure constituent A (solute atoms) and pure constituent B (solvent atoms) that having dissimilar atomic cells, are in contact with each other to form alloy A_c B_{1-c}, which has a Wigner-Seitz (WS) atomic cell (indicated in FIGURE 3.2), then there will be a electron-density discontinuity at the boundary between two different cells (atomic cells of A and B). However, as for the alloy A_c B_{1-c}, in order to enhance a energy minimum state as that of previous pure A and pure B, the discontinuity of electron density should be removed, which may result in a positive contribution to the energy of alloy system. Moreover, there will be a difference in

chemical potentials for electrons ($\Delta\phi$) in A and B two types of atomic cells when forming A_c B_{1-c}, which may lead to the transfer of charge at the boundary, and this procedure will make a negative contribution to the formation enthalpy of A_cB_{1-c} alloy [21].

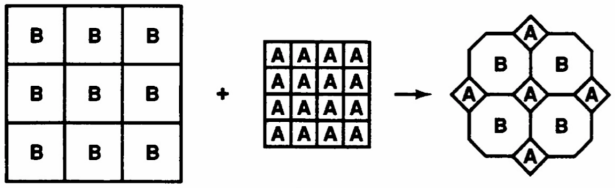

FIGURE 3.2: The Wigner-seitz atomic cell of AB alloy: the formation of an AB alloy from pure A and pure B metals [22]

Therefore, after introducing the basic theory of the Miedema model, we want to derive a expression for the formation enthalpy of binary alloy A_cB_{1-c} in bulk region. As we have mentioned above, the formation enthalpy H^{int}_{AinB} can be evaluated by two critical parameters: (1) the electron density discontinuity, $\Delta n^{1/3}_{ws}$, providing a positive contribution; (2) the electronegativity difference between two elements, $\Delta\phi$, which is defined as the difference in work functions between solute and solvent atoms, which leads to a negative contribution. However, as we want to estimate the H^{int}_{AinB} numerically, then we need to correlate it with the alloy concentration, to make it a concentration-dependent value. Thus, the formation enthalpy of statistical solid solution of bulk region can be expressed as

$$H^{form}_{bulkc} = cf^A_B H^{int}_{AinB} \tag{3.8}$$

Where, c denotes the solute (A) concentration of bulk, before GB segregation, c is taken as c_0, while after segregation, c is taken as c_1; f^A_B is the degree to which A atoms are surrounded by B atoms [22], if A is fully surrounded by atoms B, then $f^A_B = 1$. If A is partially surrounded by B atoms, then f^A_B should be modified as

$$f^A_B = c^S_B[1 + m(c^S_A c^S_B)^2] \tag{3.9}$$

Where, m is an introduced parameter, in solid solution, $m = 8$ is chosen [23]; whereas, in amorphous phase, $m = 5$ or $m = 4$ is suggested [23,24], due to the existence of chemical short-range order (CSRO). In addition, c^S_B indicates the surface fraction of B atoms [21]], c^S_A indicates the surface fraction of A atoms, their expressions are given as

$$c^S_B(c) = \frac{(1-c)V^{2/3}_B}{cV^{2/3}_A + (1-c)V^{2/3}_B} \tag{3.10}$$

$$c^S_A(c) = \frac{cV^{2/3}_A}{cV^{2/3}_A + (1-c)V^{2/3}_B} \tag{3.11}$$

In the meantime, the formation enthalpy H^{int}_{AinB} that we discussed above, will be given as

$$H^{int}_{AinB} = \frac{(V^{2/3}_A)_{alloy}}{(n^{-1/3})_{av}}[-P(\Delta\phi)^2 + Q(\Delta n^{1/3}_{ws})^2 - R] \tag{3.12}$$

$$(V^{2/3}_A)_{alloy} = (V^{2/3}_A)_{pure}[1 + \alpha f^A_B(\phi_A - \phi_B)] \tag{3.13}$$

Where, $(V_A^{2/3})_{alloy}$ stands for the surface area of solute atom A, and it should be distinguished from the surface area of pure A, this is because when forming an alloy A-B, the individual atomic volume of A or B can be influenced by the charge transfer, therefore the volume of pure A should be modified. In above equation, α is a constant, which is derived from the experimental data; $\alpha = 0.14$ for alkali metals, $\alpha = 0.1$ for divalent metals, $\alpha = 0.07$ for both noble and trivalent metals, and $\alpha = 0.04$ for all other metals [23]. Also, $\Delta\phi$ denotes the electronegativity difference ($\Delta\phi = \Delta\phi_A - \Delta\phi_B$). $\Delta n_{ws}^{1/3}$ indicates the discontinuity of the electron density. Moreover, for a binary system, $(n_{ws}^{-1/3})_{av}$ can be calculated by $(n_{ws}^{-1/3})_{av} = \frac{1}{2}(\frac{1}{(n_{ws}^{A})^{1/3}+(n_{ws}^{B})^{1/3}})$. In addition, P, Q, and R are empirical constants, which are obtained from experiments, and the ratio of the proportionality constants Q/P is konwn as 9.4 [23]. For alloys that consist of two transition metals, P is taken as 14.1 or 14.2 [24], and for alloys consisting of two non-transition metals, P is taken as 12.35 or 12.3 [24]. R is a filling factor that accounts for the filling degree of the Brillouin zones, if a binary alloy consists of two transition metals, R is taken as 0. Hence, for a binary alloy, the formation enthalpy of bulk region can be expressed as
(1) Before GB segregation

$$H_{bulkc_0} = c_0 f_B^A(c_0) \frac{V_A^{2/3}}{(n_{ws}^{-1/3})_{av}} [-P(\Delta\phi)^2 + Q(\Delta n_{ws}^{-1/3})^2 - R] \tag{3.14}$$

(2) After GB segregation

$$H_{bulkc_1} = c_1 f_B^A(c_1) \frac{V_A^{2/3}}{(n_{ws}^{-1/3})_{av}} [-P(\Delta\phi)^2 + Q(\Delta n_{ws}^{-1/3})^2 - R] \tag{3.15}$$

In the meantime, lots of experimental studies have been performed to measure the thermodynamic properties of binary alloy systems, including the formation enthalpies. According to the reference [24], Kleppa et al. and Meschel et al. measured hundreds of standard formation enthalpies of binary alloys in the past ten years. When comparing the experimental results with that calculated by using Miedema model, a statistical deviation was observed, and it was found that more than 90 % of experimental values were higher or less negative than the calculated one [24]. The deviation is more obvious when alloying elements have a large atomic size difference. Thus, in order to increase the precision of Miedema model, some modifications need to be incorporated. For example, a composition-independent atomic size difference (ASD) factor is suggested by Zhang [24]. After introducing the ASD factor, the calculated formation enthalpy seems to be improved to some extent, i.e., the enthalpy of YPd increases from –123.2 kJ/mol that predicted by original Miedema model up to –90.9 kJ/mol (after ASD is introduced), which becomes more close to the experimental value –94.9 kJ/mol. The reason behind is that ASD factor is able to lower the contact area between the two dissimilar WS cells, and to decrease the binding energy between solute and solvent atoms. The ASD factor S_c is expressed as

$$S_c = \frac{a V_A^{2/3} V_B^{2/3}}{(V_A^{2/3} + V_B^{2/3})^2} \tag{3.16}$$

Where, V_A is the molar atomic volume of solute atom A, V_B is the molar atomic volute of solvent B. Moreover, a is a empirical constant, it is taken as 3.2598 when $P = 14.2$ is satisfied; or it is taken as 3.2829 when $P = 14.1$ is satisfied.

After introducing the ASD factor, the modified formation enthalpy becomes

$$H_{bulkc_0} = S_c c_0 f_B^A(c_0) \frac{(V_A^{2/3})_{alloy}}{(n_{ws}^{-1/3})_{av}} [-P(\Delta\phi)^2 + Q(\Delta n_{ws}^{-1/3})^2 - R] \tag{3.17}$$

$$H_{bulkc_1} = S_c c_1 f_B^A(c_1) \frac{(V_A^{2/3})_{alloy}}{(n_{ws}^{-1/3})_{av}} [-P(\Delta\phi)^2 + Q(\Delta n_{ws}^{-1/3})^2 - R] \tag{3.18}$$

3.3.2 Entropy of mixing

As regards the entropy term of bulk region, if we assume the mixing entropy of a solid solution is corresponding to that of an ideal mixing, then the entropy of mixing could be derived by utilizing the standard statistical approach, where atoms are randomly distributed throughout the alloy system. Then the entropy of mixing of bulk region will be given as
(1) Before GB segregation

$$S_{bulkc_0} = -R[c_0 \ln c_0 + (1 - c_0) \ln(1 - c_0)] \tag{3.19}$$

(2) After GB segregation

$$S_{bulkc_1} = -R[c_1 \ln c_1 + (1 - c_1) \ln(1 - c_1)] \tag{3.20}$$

Where, R denotes the gas constant; c_0 indicates the solute concentration of bulk before GB segregation, and c_2 indicates the solute concentration of bulk after GB segregation.

3.3.3 Size mismatch energy

When forming a binary alloy, there generally is a size misfit between the solute and solvent atoms, which may lead to elastic deformations, and give rise some additional positive elastic strain to energy. McLean developed a model where elastic energy is the driving force for solute segregation to the grain boundary region. This this energy can be fully relieved by grain boundary segregation. An Eshelby-type continuum linear elastic theory is utilized in evaluating the change of elastic energy that attributed to the exchange of solute and solvent atoms [12]. In some alloy systems, i.e., Fe-Zr and Pd-Zr [12], both grain boundary segregation and thermodynamic stabilization phenomena are observed, this is because there is a large atomic misfit between the two distinct atoms, thus elastic energy can dominate the segregation enthalpy. When size differences are small as in Fe-Ni and Fe-Cr systems, there is no effect of Ni on the thermodynamic stabilization of Fe-Ni, whereas Cr only imposes a small effect. Therefore, when describing the free energy of bulk region, size mismatch energy should be also incorporated, and this energetic term can be evaluated by using elastic constants and the relative size difference of two constituents. For simplicity, we will assume Poisson's ratio as 0.3 for the all metals, then based on the Eshelby-type continuum linear elastic theory, the elastic strain can be expressed as

$$\Delta H_{size} = 1.25\overline{BV_m}\delta^2 c(1 - c) \tag{3.21}$$

Where, c indicates the solute concentration of bulk region, and can be taken as c_0 (before GB segregation) or c_1 (after GB segregation). $\overline{BV_m}$ indicates the average value of the product of bulk modulus and molar volume of two elements, which can be

expressed as

$$\overline{BV_m} = \frac{1}{2}(B_A V_A + B_B V_B) \tag{3.22}$$

Where, B is the bulk modulus of solute or solvent atoms. V is the molar volume of solute or solvent atoms. The δ accounts for the relative size difference between two alloy metals, which is equal to

$$\delta = \frac{2(V_A^{1/3} - V_B^{1/3})^2}{V_A^{1/3} + V_B^{1/3}} \tag{3.23}$$

Moreover, Friedel suggested another way to estimate the elastic mismatch energy of a binary alloy, which is composition-independent and can be expressed as [15]

$$\Delta H_{size} = \frac{2K_A G_B (V_A - V_B)^2}{3K_A V_B + 4G_B V_A} \tag{3.24}$$

Where, K_A is the bulk modulus of solute A atoms, whereas G_B is the shear modulus of solvent B atoms. And V_A and V_B are the atomic volumes of pure solute and solvent atoms. It is mentioned that, this energy term is always positive, therefore, it will predict the solute segregation to the grain boundary region.

3.3.4 The free energy of bulk

Thus, after discussing the definition of each energy contribution, the complete expression for the free energy of bulk region is
(1) Before GB segregation

$$\begin{aligned} G_{bulk_{c_0}} = {} & S_c c_0 f_B^A(c_0) \frac{V_A^{2/3}}{(n_{ws}^{-1/3})_{av}} [-P(\Delta\phi)^2 + Q(\Delta n_{ws}^{1/3})^2 - R] \\ & + TR[c_0 \ln c_0 + (1 - c_0)\ln(1 - c_0)] + 1.25\overline{BV_m}\delta^2 c_0(1 - c_0) \end{aligned} \tag{3.25}$$

(2) After the GB segregation:

$$\begin{aligned} G_{bulk_{c_1}} = {} & S_c c_1 f_B^A(c_1) \frac{V_A^{2/3}}{(n_{ws}^{-1/3})_{av}} [-P(\Delta\phi)^2 + Q(\Delta n_{ws}^{1/3})^2 - R] \\ & + TR[c_1 \ln c_1 + (1 - c_1)\ln(1 - c_1)] + 1.25\overline{BV_m}\delta^2 c_1(1 - c_1) \end{aligned} \tag{3.26}$$

3.4 The free energy of grain boundary region

Grain boundary region can be considered as a region, where two differently oriented crystals are contacting with each other, and some interatomic forces exist and connect the two region. Based on literature [25], two types of grain boundary structures are possible: (1) periodic structure, where atoms at the boundary form a periodic array; (2) amorphous structure, where atoms are disordered at the boundary region. The model considers the GB structure as a amorphous phase was initially developed by Rosenhain and his co-workers. The assumption was supported by some observations including the occurrences of grain boundary sliding at high temperature, plastically deformation by small stresses at higher temperature, and the grain boundary brittleness at low temperature [26]. Whereas, the most persuasive evidence was provided by Jeffries [26], who collected a lot of information regarding the

properties of amorphous and crystalline phases, he concluded the grain boundary was amorphous [27].

However, the concept of amorphous grain boundary gradually has changed. Some other models and experiments suggest that the atoms at a boundary form a periodic array, which include the dislocation models, island models, coincidence site models and the structural unit model (which is governed by a thermodynamic principle) [26]. The periodic assumption is supported by some experimental observations, i.e., in Al-Zn alloy system, the grain boundary diffusion coefficient of Zn varies as a function of the tilt angle in <110> tilt boundaries of Al; moreover, the <111> tilt boundary energies in zone refined Pd also varies as a function of tilt angle; also, anisotropic properties of grain boundary diffusion was reported for [100] tilt boundaries in Ag at 450° [28]. These facts suggest that the grain boundary properties may depend on the boundary inclination and misorientation relationship, which means the different types of grain boundaries in certain material may have different structures.

Hence, it is more reasonable to assume the grain boundary regions consist of a partial periodic structure and a partial amorphous structure, rather than assume as fully periodic or fully amorphous. In our thermodynamic model, a new parameter *del* is introduced, to indicate the degree of order for the grain boundary region (indicated in FIGURE 3.1) of the binary system.

By analogy with the analyzing method used in bulk region, the molar Gibbs free energy of GB region can be estimated in a similar way. The free energy of grain boundary region contains the contributions from four parts: (1) The enthalpy of mixing H_{gb}^{form}, which is attributed to the chemical interactions between A and B atoms, and can be estimated by using Miedema model. This part of energy has the same expression as those given in formulas 3.17 and 3.18; (2) the so called topological enthalpy H_{gb}^{top}, which accounts for the differences between the crystalline and amorphous states, and can be quantified by being correlated with the heat of fusions of each alloy components; (3) the configuration entropy; (4) the elastic mismatch energy ΔH_{size} between the solute and solvent atoms. It is mentioned that the size mismatch contribution is not important in amorphous phase, this is because atoms are not constrained to fit a certain volume. In conclusion, the expression of the total free energy of GB region can be considered as

$$G_{gb_{c_0}} = H_{gb_{c_0}}^{form} + del\ H_{gb_{c_0}}^{top} - TS_{gb_{c_0}} + (1 - del)\Delta H_{size} \tag{3.27}$$

$$G_{gb_{c_2}} = H_{gb_{c_2}}^{form} + del\ H_{gb_{c_2}}^{top} - TS_{gb_{c_2}} + (1 - del)\Delta H_{size} \tag{3.28}$$

Where, G_{gbc_0} denotes the free energy of grain boundary region before segregation, and the binary composition at current state is expressed as $A_{c_0}B_{1-c_0}$; whereas G_{gbc_2} denotes the free energy of grain boundary region after segregation. The introduced parameter *del* denotes the fraction of amorphous phase of a binary system, i.e., if $del = 0.5$, the grain boundary region is composed of a half of amorphous state and a half of solid state, therefore, both topological enthalpy and elastic mismatch will make equal contributions to the total free energy. The numerical value of *del* can be varied from 0 to 1.

3.4.1 Formation enthalpy of binary alloy

The formation enthalpy of grain boundary region contains contributions from two parts: the enthalpy of mixing and the topological enthalpy. According to the first approximation, Bakker has assumed the enthalpy of mixing of amorphous phase is equal to that of the statistical solid solution, both of them can be evaluated by using Miedema model, and the chemical interaction terms will be given as
(1) Before GB segregation

$$H_{gb_{c_0}} = S_c c_0 f_B^A(c_0) \frac{V_A^{2/3}}{(n_{ws}^{-1/3})_{av}} [-P(\Delta\phi)^2 + Q(\Delta n_{ws}^{1/3})^2 - R] \tag{3.29}$$

(2) After GB segregation

$$H_{gb_{c_2}} = S_c c_2 f_B^A(c_2) \frac{V_A^{2/3}}{(n_{ws}^{-1/3})_{av}} [-P(\Delta\phi)^2 + Q(\Delta n_{ws}^{1/3})^2 - R] \tag{3.30}$$

Where, S_c is the empirical atomic size difference factor, which is expected to improve the predicting precision of a binary alloy system. c_1 and c_2 stands for the solute concentrations of GB before and after segregation separately. f_B^A denotes the degree of surrounding of A atoms by B, and its expression is given as $f_B^A = c_B^S[1 + m(c_A^S c_B^S)^2]$. Due to the existence of chemical short-range order (CSRO) in amorphous phase, m will be chosen as 5.

As for evaluating the topological enthalpy of grain boundary region, we will adopt the method proposed by Alonso et al., the energy term can be calculated by the composition-average of heat of fusion of each alloy element, therefore, the expression will be given as
(1) Before GB segregation

$$H_{gb_{c_0}}^{top} = c_0 H_A^{fuse} + (1 - c_0) H_B^{fuse} \tag{3.31}$$

(2) After GB segregation

$$H_{gb_{c_2}}^{top} = c_2 H_A^{fuse} + (1 - c_2) H_B^{fuse} \tag{3.32}$$

Where, H_A^{fuse} and H_B^{fuse} are the heat of fusions of solute and solvent atoms.

In addition, if the mixing entropy of grain boundary region is assumed to be a random mixture, again, the statistical method can be employed [29], which generates the similar expressions as that of 3.19 and 3.20, and the only difference lies in the solute composition, where the solute concentration of GB becomes c_2 after the GB segregation. Furthermore, the size mismatch energy should be incorporated, when the grain boundary region is considered as a partial solid solution and a partial amorphous phase.

3.4.2 The free energy of grain boundary region

The total free energy of grain boundary region can be expressed as
(1) Before GB segregation:

$$G_{gb_{c_0}} = S_c c_0 f_B^A(c_0)\frac{V_A^{2/3}}{(n_{ws}^{-1/3})_{av}}[-P(\Delta\phi)^2 + Q(\Delta n_{ws}^{1/3})^2 - R] + del(c_0 H_A^{fuse} + (1-c_0)H_B^{fuse}) + TR[c_0\ln c_0 + (1-c_0)\ln(1-c_0)] + (1-del)1.25\overline{BV_m}\delta^2 c_0(1-c_0) \tag{3.33}$$

(2) After the GB segregation:

$$G_{gb_{c_2}} = S_c c_2 f_B^A(c_2)\frac{V_A^{2/3}}{(n_{ws}^{-1/3})_{av}}[-P(\Delta\phi)^2 + Q(\Delta n_{ws}^{1/3})^2 - R] + del(c_2 H_A^{fuse} + (1-c_2)H_B^{fuse}) + TR[c_2\ln c_2 + (1-c_2)\ln(1-c_2)] + (1-del)1.25\overline{BV_m}\delta^2 c_2(1-c_2) \tag{3.34}$$

3.5 The free energy of the interfacial area

In this model, the volume of grain consists of two regions, one belongs to the bulk, the other belongs to the grain boundary, and a interface exists at the contact area between these two regions (indicated in figure 1). The atomic interactions have already uniquely defined in bulk and GB regions. When grain boundary segregation occurs, the alloy compositions A_cB_{1-c} in both of the two regions are no longer the same, which may lead to some changes in degree of atomic interactions, therefore it is necessary to introduce an additional energetic term to capture the energy between the bulk and GB regions, ant this term is called as interfacial energy, which will be represented by γ.

The interfacial energy γ can be estimated as follows. We consider the bulk region as a solid solution, the grain boundary region as a partial amorphous phase (in a ratio of *del*) and a partial solid solution (in a fraction of $1-del$), therefore, two types of interfaces are possible, including a solid-solid interface, $<A_cB_{1-c}> - <A_cB_{1-c}>$, and a solid-amorphous interface, $<A_cB_{1-c}> - \{A_cB_{1-c}\}$. Both of the two interfaces will make contributions to the total interfacial energy, however, with a different weight. The weight of each type will be determine by the fraction of solid solution (*del*) and the fraction of amorphous phase ($1-del$) in grain boundary region. Therefore, the full expression of the interfacial energy will be given as
(1) Before GB segregation

$$\gamma_{00} = (1-del)\gamma_{<A_{c_0}B_{1-c_0}>-<A_{c_0}B_{1-c_0}>} + del\gamma_{<A_{c_0}B_{1-c_0}>-\{A_{c_0}B_{1-c_0}\}} \tag{3.35}$$

(2) After GB segregation

$$\gamma_{12} = (1-del)\gamma_{<A_{c_1}B_{1-c_1}>-<A_{c_2}B_{1-c_2}>} + del\gamma_{<A_{c_1}B_{1-c_1}>-\{A_{c_2}B_{1-c_2}\}} \tag{3.36}$$

Where, γ_{00} denotes the total interfacial energy of interface before GB segregation, whereas γ_{12} denotes the total interfacial energy of interface after GB segregation.

The parameter *del* indicates the fraction of amorphous phase of grain boundary region. Moreover, $\gamma_{<A_cB_{1-c}>-<A_cB_{1-c}>}$ represents the interfacial energy of the solid-solid interface, whereas, $\gamma_{<A_cB_{1-c}>-\{A_cB_{1-c}\}}$ represents the interfacial energy of the solid-amorphous interface.

In following content, the derivations of interfacial energy of each type will be discussed.

3.5.1 The interfacial energy of a solid-solid interface

The interfacial energy of a solid-solid interface can be attributed to the energy differences between the $< A_cB_{1-c} >$ (of bulk) and $< A_cB_{1-c} >$ (of GB, in a ratio of *del*) two phases. And the energy contains contributions from two parts: (1) the chemical interactions between solute and solvent atoms at the interface, $\gamma^{interaction}_{<A_cB_{1-c}>-<A_cB_{1-c}>}$; (2) the mismatch energy, $\gamma^{mismatch}_{<A_cB_{1-c}>-<A_cB_{1-c}>}$, which is contributed from the strain that arising from the mismatch at the interface between two lattices. Therefore the full expression of interfacial energy of solid-solid interface will be given as

$$\gamma_{<A_cB_{1-c}>-<A_cB_{1-c}>} = \gamma^{interaction}_{<A_cB_{1-c}>-<A_cB_{1-c}>} + \gamma^{mismatch}_{<A_cB_{1-c}>-<A_cB_{1-c}>} \tag{3.37}$$

3.5.1.1 The interaction energy of solid-solid interface

The interfacial energy that contributed from the atomic interactions can be evaluated by following method. If A atoms are completely surrounded by B atoms, then the increase of enthalpy would be given as H^{int}_{AinB} per mole A atoms (contained in certain phase) in an infinitely dilute system [22]. However, at the interface, only a surface fraction of A atoms (c^S_A) are in contact with B, therefore, the increase of enthalpy that attributed to the A atoms that locating at the interface should be modified into $c^S_A H^{int}_{AinB}$. Furthermore, the interaction energy of interface is defined as the enthalpy increase per unit area, therefore, the enthalpy increase $c^S_A H^{int}_{AinB}$ should be divided by the area $c^S_A g V_A^{2/3}$ that being occupied by these surface A atoms, and g is a constant that relying on the shape of Wigner-Seitz cell of A, which is approximately equal to 4.5×10^8. Hence, we can draw the following conclusion: If A atoms are fully surrounded by B, then the interfacial energy that resulted from the chemical interactions at the interface would be given as $H^{int}_{AinB}/gV_A^{2/3}$ per mole A atoms within a certain phase in an infinitely dilute system.

However, in binary alloy systems that we discussed, A atoms are not completely surrounded by B, and the alloy system is non-dilute. Therefore, the parameter f^A_B will be incorporated to measure the degree that how many A atoms are surrounded by B. Besides, the enthalpy increase $c^S_A H^{int}_{AinB}$ (mentioned before) should be correlated with the solute concentration of each phase. Thus, the final expression of the solid-solid interfacial energy that attributed to atomic interactions will be
(1) Before GB segregation

$$\gamma^{interaction}_{<A_{c_0}B_{1-c_0}>-<A_{c_0}B_{1-c_0}>} = \frac{c_0 f^A_B(c_0) H^{int}_{AinB}}{g V_A^{2/3}} + \frac{c_0 f^A_B(c_0) H^{int}_{AinB}}{g V_A^{2/3}} \tag{3.38}$$

(2) After GB segregation

$$\gamma^{interaction}_{<A_{c_1}B_{1-c_1}>-<A_{c_2}B_{1-c_2}>} = \frac{c_1 f^A_B(c_1) H^{int}_{AinB}}{g V_A^{2/3}} + \frac{c_2 f^A_B(c_2) H^{int}_{AinB}}{g V_A^{2/3}} \tag{3.39}$$

Where, the first energy terms in both equations are contributions from the chemical interactions between A and B atoms at the interface, when we assume the solute concentration of GB region approaches to 0; whereas the second energy terms are contributed from the atomic interactions, when we assume the solute concentration of bulk region approaches to 0.

3.5.1.2 The mismatch energy of solid-solid interface

In the meantime, the mismatch at the interface between two lattices, will also contribute to the interfacial energy, and this part of energy can be estimated by the following form
(1) Before GB segregation

$$\gamma^{mismatch}_{<A_{c_0}B_{1-c_0}>-<A_{c_0}B_{1-c_0}>} = \frac{1}{3}\left(\frac{\gamma_{<A_{c_0}B_{1-c_0}>} + \gamma_{<A_{c_0}B_{1-c_0}>}}{2}\right) \tag{3.40}$$

(2) After GB segregation

$$\gamma^{mismatch}_{<A_{c_1}B_{1-c_1}>-<A_{c_2}B_{1-c_2}>} = \frac{1}{3}\left(\frac{\gamma_{<A_{c_1}B_{1-c_1}>} + \gamma_{<A_{c_2}B_{1-c_2}>}}{2}\right) \tag{3.41}$$

Where, $\gamma_{<A_cB_{1-c}>}$ (c is taken as c_0, c_1 or c_2) indicates the surface energy of a mixing phase. And the expression for the surface energy can be derived as follows. If we assume that a binary crystal A_cB_{1-c} is fractured, then additional new surfaces will be created, in the meantime, some bond pairs that crossing the surface would break, these changes can lead to some energy increases of the alloy system, which is equivalent to the surface energy of this mixing phase. Before the bonds broken, there are four types of bonds including A-A, B-B, A-B and B-A bond pairs, and the fraction of each type can be estimated by the product of the surface fractions of two atoms (c_A^A or c_B^S) involved in the certain bond that we considered, i.e., the fraction of B-B bonds is $(c_B^S)^2$. After the fracture, two new surfaces will be generated, atoms located at the surface will interact with vacuum. The energy increases that contributed from A-A and B-B bonds can be evaluated by using the surface energies of atoms A and B accordingly. Whereas, the energy increases that attributed from A-B and B-A bonds can be evaluated by using $H^{int}_{AinB}/gV^{2/3}_{V_A}$ for each of them [30]. Therefore, we can express the surface energy of A_cB_{1-c} as the following form

$$\gamma_{<A_cB_{1-c}>} = c_A^S(c)\gamma_A + c_B^S(c)\gamma_B - 2c_A^S(c)c_B^S(c)\frac{H^{int}_{AinB}}{gV_A^{2/3}} \tag{3.42}$$

Where, the first two terms on the right represent the interaction energy between the A(B) atoms and vacuum, which originates from the breakage of A-A and B-B bonds separately, whereas the last term is contributed from the breakage of A-B and B-A bonds. In addition, γ_A denotes the surface energy of A atoms, γ_B denotes the surface energy of B atoms.

3.5.2 The interfacial energy of a solid-amorphous interface

Because we consider the bulk as a solid solution, grain boundary region as a partial solid solution and a partial amorphous phase, therefore, besides the solid-solid interface, there is also a solid-amorphous interface, and its interfacial energy can be derived in the following way.

At the solid-amorphous interface, $< A_cB_{1-c} > -\{A_cB_{1-c}\}$, there are several types of bonds A-A, B-B, A-B and B-A crossing the interface and bridging the two different regions, which are associated with an energy increase of the system, and the energy increase will be defined as the interfacial energy of the solid-amorphous interface. It contains the contributions from three parts, one is related to the enthalpy increase that arising from the solid solution at the interface (bulk region), one is related to the entropy increase that arising from the amorphous phase at the interface (GB region), and the other is related to the atomic interactions at the interface. Thus, the full expression will be given as

$$\gamma_{<A_cB_{1-c}>-\{A_cB_{1-c}\}} = \gamma^{enthalpy}_{<A_cB_{1-c}>-\{A_cB_{1-c}\}} + \gamma^{entropy}_{<A_cB_{1-c}>-\{A_cB_{1-c}\}} + \gamma^{interaction}_{<A_cB_{1-c}>-\{A_cB_{1-c}\}} \tag{3.43}$$

3.5.2.1 The enthalpy contribution of solid-amorphous interface

The enthalpy contribution to the interfacial energy resulting from the solid solution of bulk at the interface. It can be estimated by correlating with fusion enthalpies of H_A^{fuse} and H_B^{fuse} per mole A and per mole B atoms respectively [30], originating from the liquid bonds A-A and B-B.
(1) Before GB segregation

$$\gamma^{enthalpy}_{<A_{c_0}B_{1-c_0}>-\{A_{c_0}B_{1-c_0}\}} = c_0\frac{H_A^{fuse}}{gV_A^{2/3}} + (1-c_0)\frac{H_B^{fuse}}{gV_B^{2/3}} \tag{3.44}$$

(2) After GB segregation

$$\gamma^{enthalpy}_{<A_{c_1}B_{1-c_1}>-\{A_{c_2}B_{1-c_2}\}} = c_1\frac{H_A^{fuse}}{gV_A^{2/3}} + (1-c_1)\frac{H_B^{fuse}}{gV_B^{2/3}} \tag{3.45}$$

3.5.2.2 The entropy contribution of solid-amorphous interface

The entropy contribution can be evaluated by using a structural model that proposed by Spaepen et al [31]. According to the structural model, a solid-amorphous interface is developed, and the configurational entropy of solid will not change, whereas only the entropy of liquid will change. The configurational entropy at the liquid side is likely to be lowered, this is because the existence of chemical short-range order (CSRO). The change in configurational entropy will lead to a positive contribution to the interfacial energy, and the expression will be given as
(1) Before GB segregation

$$\gamma^{entropy}_{<A_{c_0}B_{1-c_0}>-\{A_{c_0}B_{1-c_0}\}} = c_0\frac{1.9RT}{gV_{AB}^{2/3}} + (1-c_0)\frac{1.9RT}{gV_{AB}^{2/3}} \tag{3.46}$$

(2) After GB segregation

$$\gamma^{entropy}_{<A_{c_1}B_{1-c_1}>-\{A_{c_2}B_{1-c_2}\}} = c_2\frac{1.9RT}{gV_{AB}^{2/3}} + (1-c_2)\frac{1.9RT}{gV_{AB}^{2/3}} \tag{3.47}$$

Where, R is the gas constant, T is the temperature at current state. V_{AB} indicates the molar volume of the binary alloy. It is mentioned that the entropy contributions at interface are attributed to the amorphous grain boundary region.

3.5.2.3 The interaction contribution of solid-amorphous interface

The interaction contribution can be attributed to the atomic interaction between A and B atoms at the interface. And the expression for this energetic term can be obtained by analogy with that discussed in the former section (the interaction energy of solid-solid interface). Therefore, the interaction contribution of interfacial energy can be expressed as
(1) Before GB segregation

$$\gamma^{interaction}_{<A_{c_0}B_{1-c_0}>-\{A_{c_0}B_{1-c_0}\}} = \frac{c_0 f_B^A(c_0) H^{int}_{AinB}}{g V_A^{2/3}} + \frac{c_0 f_B^A(c_0) H^{int}_{AinB}}{g V_A^{2/3}} \tag{3.48}$$

(2) After GB segregation

$$\gamma^{interaction}_{<A_{c_1}B_{1-c_1}>-\{A_{c_2}B_{1-c_2}\}} = \frac{c_1 f_B^A(c_1) H^{int}_{AinB}}{g V_A^{2/3}} + \frac{c_2 f_B^A(c_2) H^{int}_{AinB}}{g V_A^{2/3}} \tag{3.49}$$

So far, all the necessary energetic expressions that involved in describing the individual free energies of bulk, grain boundary regions and the interfacial area, have already been clearly definedbut in different units. Therefore, if we substitute these energy terms into equation 3.4 and 3.5, and impose some transformations, then we will determine the total change of free energy of the binary system that resulted from the solute segregation to grain boundaries.

3.6 The total change of free energy of the binary system

For a cubic-shaped binary alloy system (FIGURE 3.1), the total free energy of the system consists of contributions from three parts: bulk region, GB region and the interfacial area. By taking the volume fractions of bulk and GB region into account, the free energy of bulk G_{bulk} and free energy of GB region G_{gb} can be weighted by the fraction of individual region, which aims at normalizing the total energy of a binary system, and limiting our discussions within certain scale range. It is mentioned that the units of G_{bulk} and G_{gb} are kJ/mol, whereas the unit of interfacial energy is kJ/m^2, therefore, in order to unify all units into kJ/mol, a conversion should be employed for the interfacial energy term. Then we have the following expressions
(1) Before GB segregation

$$G^1_{total} = f_{bulk} G_{bulkc_0} + f_{gb} G_{gbc_0} + \gamma_{00} V c_0^{2/3} \tag{3.50}$$

(2) After GB segregation

$$G^2_{total} = f_{bulk} G_{bulkc_1} + f_{gb} G_{gbc_2} + \gamma_{12} V c_0^{2/3} \tag{3.51}$$

where, G^1_{total} is the total free energy of binary system before segregation, whereas G^2_{total} is the total energy after segregation. $V_{c_0}^{2/3}$ denotes the surface area of alloy $A_{c_0}B_{1-c_0}$, and the purpose of multiplying this term is to ensure a consistent unit, kJ/mol. Later, the energetic changes of the alloy system that attributed to the enrichment of solute atoms at the grain boundary region can be given as

$$\Delta G_{total} = G^2_{total} - G^1_{total} \tag{3.52}$$

Based on the calculated results of ΔG_{total}, we can determine whether solute atoms prefer to segregate into the grain boundary region, or prefer to stay in the interior of bulk. If $\Delta G_{total} < 0$ is satisfied, grain boundary segregation will occur, because the binary system wants to minimize its free energy, whereas if $\Delta G_{total} > 0$ is satisfied, then the system will prefer to remain at the current state, therefore nothing could happen. If we plot the ΔG_{total} with respect to the solute concentration in GB region c_2, then the fitting curve will provide us information about the minimum ΔG_{total}, as well as its corresponding equilibrium solute concentration c_2.

3.7 Grain boundary energy of the binary alloy system

For a nanocrystalline binary alloy, solute segregation to grain boundary regions can lower the effective grain boundary energy of the alloy system γ_{gb} and thus reduce the driving force for grain growth. If γ_{gb} is decreased to 0, all the driving forces will be completely eliminated, then there exists a metastable equilibrium grain size, which only has a week temperature dependence. According to the reference [32], one way of deriving the effective grain boundary energy of the binary alloy has been introduced, and the expression is given as

$$\gamma_{gb} = \gamma_{gb0} + \Gamma \Delta G_{total} \tag{3.53}$$

Where, γ_{gb0} stands for the grain boundary energy of pure solvent atom, which can be estimated by 1/3 of surface energy of pure metal component. Γ stands for the excess amount of segregated solute per unit area on the grain boundaries, which describes the differences in solute concentrations of bulk interior and the grain boundary region. ΔG_{total} stands for the changes of Gibbs free energy that being attributed to the solute segregation. However, the equation above is derived under a dilute limit assumption by assuming the McLean type segregation, whereas in this thermodynamic model, alloy system is considered as a regular solid solution without being restricted to the dilute system. Therefore, the effective grain boundary energy solved from Eq.3.53 may, not be precise enough, but at least it can be treated as a feasible method to make a rough estimation. In addition, based on reference [17], the solute excess can be derived by considering the distribution of atoms within a system, and it can be expressed as

$$\Gamma = \frac{t(c_2 - c_1)}{V_B(1 - c_1)} \tag{3.54}$$

Where, t denotes the grain boundary thickness; c_1 denotes the solute concentration of bulk region after segregation, whereas c_2 denotes the solute concentration of GB region after segregation; V_B denotes the molar volume of solvent atoms. According to Eq.3.53, if the product of Γ and ΔG_{total} is negative, then the effective grain boundary energy of binary alloy, γ_{gb}, will be lower than that of pure metal, γ_{gb0}, which may suggest the grain growth of alloy system can be decreased by solute segregation, in the meantime, if $\Gamma \Delta G_{total}$ is negative enough to cancel out γ_{gb0} ($\gamma_{gb} = 0$), then the nanocrystalline alloy will reach a thermodynamically stable grain size, and grain growth phenomenon will be fully inhibited. However, if the product of Γ and ΔG_{total} is positive, then the grain growth will not be restrained by solute segregation to GB region.

Chapter 4

Analysis of calculation results

In this chapter, several different types of metallic binary alloys will be investigated, aiming at exploring the adaptability and predictability of this GB segregation model. These alloys are given as: Pd-Cu, Pd-Ag, Pd-Zr, Pd-Y, Pd-Fe, Fe-Zr, Ti-Cu, Y-Fe, Ni-W and Nb-Cu. Their simulation results will be compared with those reported in the literature, thus to verify the feasibility of this model. Among them, Pd-Cu binary alloy shows some advantages. For example, Pd-Cu alloy membrane is relatively cheap when compared with other types of Pd-based alloys, i.e., Pd-Ag, Pd-Ni, Pd-Au and Pd-Ru [33], and it can exhibit a higher H_2 permeability, due to the formed bcc structure when the Cu concentration is between 30 and 60 wt% [33]. Moreover, Pd-Cu thin film shows good performance in resisting the hydrogen sulfide and sulfurous constituents during the applications in hydrogen separation membranes and coal gasification [34]. According to Mcknly and Nitro, Pd-Cu thin film also shows a strong thermal resistance at elevated temperature without suffering detectable physical changes [35]. Therefore, in the parametric study section, only the Pd-Cu alloy will be treated, and we will determine how the alloy's segregation tendency and the thermodynamic stability are influenced by the variations of different parameters, including the initial solute concentration c_0, the grain size D, the grain boundary thickness t, the annealing temperature T, and the fraction of amorphous phase in grain boundary region del.

4.1 Grain boundary segregation model applied to different binary alloys–Modelling results

In order to verify the generality of the grain boundary segregation model, in this section, the model will be applied to the various metallic A-B alloys (A:solvent atom; B: solute atom), including Pd-Cu, Pd-Ag, Pd-Zr, Pd-Y, Pd-Fe, Fe-Zr, Ti-Cu, Y-Fe, Ni-W and Nb-Cu. They may show distinct performances in the solute segregation to grain boundary, thus leading to the different behaviours in the segregation-introduced thermodynamic stability. The reason for the selections lies in the fact that these alloys are reported to show the segregation-introduced stabilization by the solute additions [12]. Before performing the calculations, we need to set the initial conditions for all of them, where these alloys will be simulated under the same condition: $c_0 = 0.3$, $D = 20nm$, $t = 0.5nm$, $T = 800K$, $m = 5$ for GB region, $m = 8$ for bulk region, $del = 0.5$ (which indicates the ratio of amorphous phase in GB region accounts for 50%). The calculation results are given as

Various binary alloys	Segregated atom	c_2 (Equilibrium)	ΔG_{total} (kJ/mol)	Effective GB energy (mJ/mol)	GB energy of solvent (mJ/mol)
Pd-Cu	Cu	0.33	-0.000527	683	683
Pd-Ag	Ag	0.55	-0.065322	682	683
Pd-Zr	Zr	≈1	-0.555997	647	683
Pd-Y	Y	≈1	-3.11598	510	683
Pd-Fe	Pd	0.29	-0.000119	683	683
Pd-Zr	Zr	≈1	-2.008923	685	825
Y-Fe	Fe	≈1	-1.846505	329	375
Ti-Cu	Ti	0.21	-0.004895	700	700
Ni-W	W	≈1	-0.401194	787	816
Nb-Cu	Cu	0.94	-0.296791	887	900

TABLE 4.1: The modelling results of different binary alloys

Where, according to this table, we can determine which type of alloy constituent prefers to segregate, and whether the segregation could lower the grain boundary energy of the host element, then we may determine the thermodynamic stability of this alloy. Based on the calculations, we find Pd-Cu, Pd-Ag, Pd-Zr, Pd-Y, Fe-Zr, Y-Fe, Ni-W and Nb-Cu exhibit the solute segregation tendency (at $T = 800K$, $c_0 = 0.3$), among them, the Pd-Zr, Pd-Y, Fe-Zr, Y-Fe, Ni-W and Nb-Cu alloys show the strong solute segregation, which is supported by the calculated equilibrium c_2 at grain boundary region, where the simulated equilibrium c_2 is larger than 90 wt%. The strong solute segregation to grain boundary region can drive the ΔG_{total} towards a more negative value, then the alloy's effective grain boundary energy γ_{gb} can be further decreased and become lower than the GB energy of solvent atoms. However, it is mentioned that the driving forces for the grain growth of these alloys can not be fully inhibited, this is because the calculated effective grain boundary energies are still much larger than 0 (When the effective GB energy equals to 0, then the alloy's grain size will become stable [36]). For Pd-Cu alloy, it shows a weak solute segregation to GB region, based on the calculation, the grain size can not be stabilized by the segregation process. For Pd-Ag, the degree of Ag segregation is relatively higher than the segregation of Cu in Pd-Cu alloy. For Ti-Cu alloy, the simulation result predicts the occurrence of the solvent segregation ($c_2 = 0.21$, which is less than the initial solute concentration in GB $c_0 = 0.3$). The GB energy of solvent Ti can not be lowered by the solvent (Ti) segregation to GB region, thus indicating the grain size of Ti-Cu may not be stabilized when sample is annealed at 800 K. However, it is mentioned that when the annealing temperature is low, i.e., $T = 400K$, $500K$, in Ti-Cu alloy, the solute segregation will occur, and when $T = 600K$, no segregation will be observed. For Pd-Fe, the calculated c_2 is equal to 0.29, which is close to the initial solute concentration of GB region (c_0=0.3), thus we may deduce that no segregation occurs in Pd-Fe at $800K$. However, in order to verify the predictability of this GB segregation model, these simulated results should be compared with those from the literature. In next section, the comparisons between the theoretical and reference results will be displayed.

4.2 The comparisons between the calculation and the literature results

According the reference [37], both the Cu (in Pd-Cu) and Ag (in Pd-Ag) atoms show the solute segregation to their grain boundaries. When $T = 600K$, it is reported that the Cu shows a weak segregation tendency, whereas, Ag shows a relatively strong segregation tendency [37]. And our simulation results meet with the conclusion mentioned above. If we set the following initial condition: $c_0 = 0.3$, $D = 20nm$, $t = 0.5nm$, $T = 600K$, $del = 0.5$, we obtain the simulated equilibrium c_2 of Pd-Cu is equal to 0.46, and its corresponding ΔG_{total} is equal to -0.008903 kJ/mol. Whereas for Pd-Ag, the simulated c_2 is equal to 0.63, and the lowest ΔG_{total} is equal to -0.075741 kJ/mol. Therefore, based on the model, we find the segregation of Ag in Pd-Ag is indeed stronger than the segregation of Cu in Pd-Cu under the same initial condition, which is in accordance with the literature report.

For Pd-Zr alloy, according to the reference[16], the Pd-Zr alloys that produced by ball milling technique was investigated by Krill et al., he found that the obvious grain size stabilization was attributed to the GB segregation of Zr, the 50 nm grain size of Pd-Zr keeps stable until $1500^{\circ}C$. The modeling results can be compared with those mentioned above. In the GB segregation model, if we set $D = 50nm$, $T = 1773K$, $c_0 = 0.3$, $t = 0.5nm$, $del = 0.5$, we will obtain the simulated equilibrium $c_2 = 0.56$, and its corresponding lowest $\Delta G_{total} = -0.144883$ kJ/mol, the effective grain boundary energy $\gamma_{gb} = 680mJ/mol$. The modelling results predict the Zr segregation to GB region, the grain growth of Pd-Zr can be slightly reduced, but can not be fully inhibited. However, in another reference [36], it observes that the grain growth stability of annealed sample $Pd_{0.81}Zr_{0.19}$ (above $600^{\circ}C$) has been improved when compared with pure Pd, but the stabilization performance is not as significant as suggested by the XRD result. And they deduce the grain size stabilization (compared with Pd) is associated with the Zr's kinetic mechanism. Therefore, based on these reasons, we may deduce that our GB segregation model could successfully predict the solute segregation tendency at GBs, but may not predict the alloy's stability in a precise way. This could be attributed our simplified assumption that we neglect the formation of secondary or intermetallic phases, and only consider a single phase. But this assumption can not always be fulfilled in the real application, where the formation of intermetallic or secondary phase may exert huge influences in the kinetic stabilization mechanism.

For Pd-Y alloy, in the reference [8], the addition of 10 wt% of Y to the Pd can stable this alloy against grain growth up at 400°C, via the GB segregation of Y, and the addition of Y in host Pd can inhibit the α to β phase transition. The investigator finds the sample $Pd_{0.9}Y_{0.1}$ has the equilibrium solubility 8 wt% (in bulk) at $400^{\circ}C$. Moreover, the formation of Pd_3Y intermetallic phase is observed, and Y prefers to incorporate into its lattice, and further stabilize the grain size. In order to verify the feasibility of the grain boundary segregation model, the theoretical calculation is performed on $Pd_{0.9}Y_{0.1}$ at 638 K, with $D = 20nm$, $t = 0.5nm$, $del = 0.5$, where based on the calculation results, we find Y shows strong segregation to GBs to lower the effective GB energy. The simulated effective grain boundary energy of Pd-Y is equal to $\gamma_{gb} = 527mJ/mol$, which is much less than the GB energy of pure Pd $\gamma_{gb} = 683mJ/mol$, indicating the segregation of Y may effectively stable the grain size to some extent.

For Pd-Fe alloy, according to the reference [9], they find the 30 wt% of Fe in Pd samples does not exhibit the grain growth until after 400°C. In the GB segregation model, for $Pd_{0.7}Cu_{0.3}$ alloy, when T=800K, the calculated equilibrium c_2 of GB region is equal to 0.29, thus implying that almost no segregation occurs, then the grain growth can not be inhibited. However, if $Pd_{0.7}Cu_{0.3}$ alloy is annealed at 500 K, based on this GB segregation model, the solute (Fe) segregation to grain boundary occurs (c_2=0.45>0.3), the grain growth can be inhibited to some extent. These conclusions meet with the report from the literature.

For other alloys, Fe-Zr (which can be analogy to Pd-Zr) [16], Ti-Cu [31], Y-Fe [38], Ni-W [12], and Nb-Cu [12], the solutes segregation introduced grain size stability is reported for all of them, however, for some of these alloys, the influences of intemetallic or secondary phases on grain size stability are observed.

Based on these analysis, we can conclude that the grain boundary segregation model could successfully predict the segregation tendency for certain type of alloy, which is comparable to those in the literature. However, the ability of predicting the grain size stability is relatively poor, which may due to the simplified assumption that we neglect the influence of intermetallic or secondary phase, and only consider a single phase. However, these extra phases may accompany some additional thermodynamic potentials that also affect the energy of the alloy system.

4.3 Parametric study

4.3.1 The influences of initial solute concentration c_0 in Pd-Cu system

As mentioned in previous chapter, we assume a closed binary alloy system, therefore, the total number of atoms within the alloy system should be fixed. All the atoms are satisfied with the conservation law, which means the concentration of bulk after GB segregation, c_1, and the solute concentration of grain boundary after GB segregation, c_2, need to be coupled with the global initial solute concentration before segregation, c_0, by a volume-fraction weight average, the relationship among c_0, c_1 and c_2 are given as

$$c_0 = f_{bulk}c_1 + f_{gb}c_2 \tag{4.1}$$

Where, f_{bulk} denotes the volume fraction of bulk region, which is defined as $f_{bulk} = [(D-t)/D]^3$, whereas, f_{gb} denotes the volume fraction of grain boundary region, which can be expressed as $f_{gb} = 1 - f_{bulk}$. During the theoretical calculations, c_2 is set as a variable that vary from 0 to 1, which suggests a growing number of solute atoms segregate to the grain boundary regions. Then c_1 can be directly solved by applying Eq.4.1, the expression of c_1 is

$$c_1 = \frac{c_0 - f_{gb}c_2}{f_{bulk}} \tag{4.2}$$

It is mentioned that the above equation contains a implied condition that c_1 should be always positive, therefore, we obtain the following inequality

$$c_0 - f_{gb}c_2 > 0 \tag{4.3}$$

Because f_{gb} relies on D and t, it is obvious that parameters c_0, D, t and c_2 will be coupled with each other via the above inequality. Therefore, before discussing the influences of c_0, other variables should be initially assigned in the Pd-Cu alloy system: $t = 0.5nm$, which is equivalent to two atomic layers; $T = 500K$; $m = 5$ for grain boundary region, which suggests the existence of short-range order, whereas $m = 8$ for bulk region; $del = 0.5$, which indicates that there is a 50% fraction of amorphous phase in GB region. As for c_0, it will be taken as 0.1, 0.2, 0.3 and 0.4. When c_0 is chosen as 0.1, according to Eq.4.3, f_{gb} should fulfill certain conditions to ensure c_1 is larger than 0: $0.1 < f_{gb} < 1$ (c_2 varies from 0 to 1). Because we have assumed the grain boundary thickness t as 0.5 nm, then we can deduce the grain size D should be larger than 14.49 nm to ensure a positive c_1. Again, if $c_0 = 0.2$, then the grain size should be larger than 7nm; if $c_0 = 0.3$, D should be larger than 5 nm; if $c_0 = 0.4$, D should be larger than 3.2 nm. Therefore, we will consider the grain size of Pd-Cu alloy system as 20 nm. So far, all the demanded variables that involved in determining ΔG_{total} have already been defined. Thus, we can determine how the ΔG_{total} of Pd-Cu system is affected by the variation of c_2 under the different c_0 conditions, and the ΔG_{total} vs c_2 plots will be made.

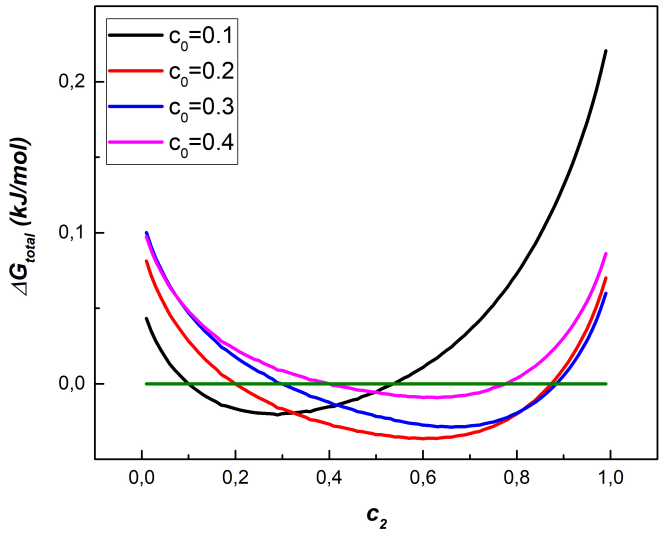

FIGURE 4.1: The ΔG_{total} vs c_2 plots correspond to the different c_0 (Green line indicates $\Delta G_{total} = 0$)

Pd-Cu	c_2 (Equilibrium)	ΔG_{total} (kJ/mol)	Effective GB energy (mJ/mol)
$c_0 = 0.1$	0.29	-0.020654	683
$c_0 = 0.2$	0.6	-0.036324	682
$c_0 = 0.3$	0.66	-0.028722	682
$c_0 = 0.4$	0.63	-0.009186	683

TABLE 4.2: The influences of c_0 on equilibrium c_2, minimum ΔG_{total} and GB energy of Pd-Cu alloy

Where, according to the above figure, it is clear that each fitted line exhibits a parabolic trend, with the increasing of c_2, ΔG_{total} initially decreases until reaching the lowest

energy point, then it will increase reversely. The procedure suggests the Gibbs free energy of Pd-Cu alloy system indeed can be reduced by solute segregation to grain boundary region. If $c_0 \leq 0.3$, with the increasing of initial solute concentration c_0, the equilibrium solute concentration c_2 (that corresponds to the minimum ΔG_{total}) will shift towards the positive direction of x-axis. If $c_0 > 0.3$, then the increasing of c_0 will lead to a reduction in equilibrium c_2, where it decreases from 0.66 to 0.63. In general, if $c_0 > 0.2$, the degree of solute segregation to GB will decrease, which means the solute atoms will prefer to stay in the bulk interior and form mixture with solvent atoms. Furthermore, we find the calculated grain boundary energies of $Pd_{1-c}Cu_c$ are almost equivalent to that of pure Pd (the 1/3 of surface energy: 683.33 mJ/m^2), which suggests the driving force of grain growth for Pd-Cu alloy may not be effectively eliminated by solute segregation to GB region, which can be attributed to the small changes in the total free energy of system after GB segregation.

4.3.2 The influences of grain size D in Pd-Cu system

In this GB segregation model, both the volume fractions of bulk f_{bulk} and grain boundary region f_{gb} are dependent on the grain size D of this alloy system. The solute concentration c_1 can be solved from Eq.4.2, which is associated with f_{bulk} and f_{gb}, thus with D. Therefore, the variation of grain size D may also exert significant influences on the Gibbs free energy of the system. In this case, D will be considered as a variable that change from 6 nm up to 100 nm (because the selection of D should be satisfied with Eq.4.3, when $c_0 = 0.3$, D should be larger than 5 nm). It is mentioned that we consider the initial solute concentration as 0.3 both because of its relevance of the purification application and because the alloy only exists in a single phase at $T = 500K$. For other input parameters, they will be assigned as follows: $c_0 = 0.3$, $t = 0.5nm$, $T = 500K$, $m = 5$ for GB region, $m = 8$ for bulk, and $del = 0.5$. The calculation result is given as

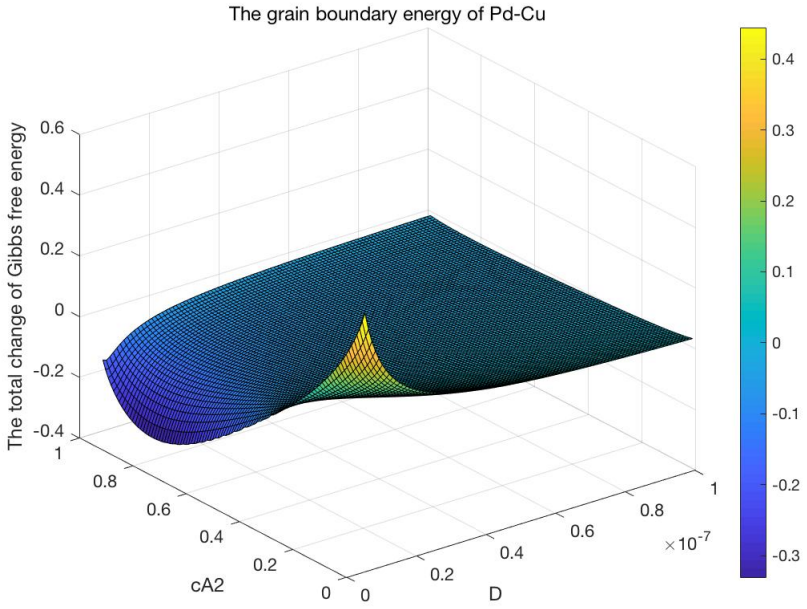

FIGURE 4.2: The influences of D on solute segregation behaviors of Pd-Cu alloy

Where, according to the plot, it is obvious that if the grain size D is small, then the solute atoms (Cu) will show a strong segregation tendency to lower the free energy of system, whereas if D approaches 100 nm, ΔG_{total} will be close to 0, which implies the segregation of Cu atoms is not likely to occur. In general, the numerical values of minimum ΔG_{total} will raise with the increasing of c_2.

Moreover, in order to have an intuitive understanding about the variations of ΔG_{total} with respect to c_2, we can also make the two dimensional ΔG_{total} vs c_2 plots that correspond to the different grain sizes D, where D will be taken as the discrete values: 10 nm, 30 nm, 50 nm and 100 nm, and the plots will be given as

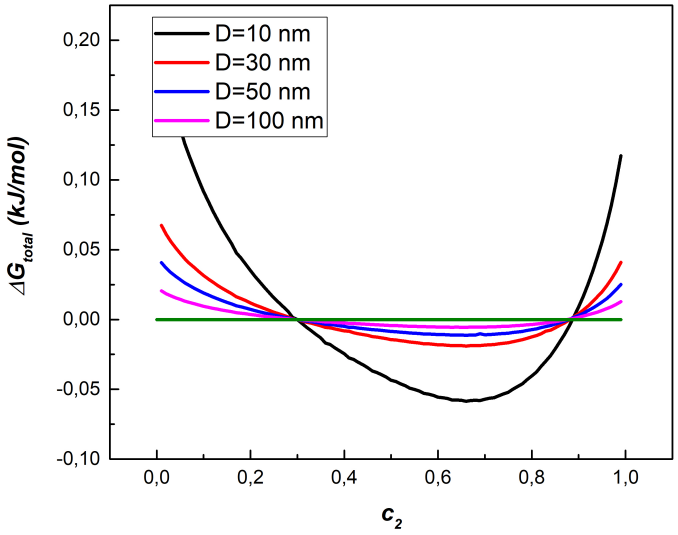

FIGURE 4.3: The ΔG_{total} vs c_2 plots correspond to the different values of grain size D (Green line indicates the $\Delta G_{total} = 0$)

Pd-Cu	c_2 (Equilibrium)	ΔG_{total} (kJ/mol)	Effective GB energy (mJ/mol)
D=10 nm	0.66	-0.058628	682
D=20 nm	0.66	-0.028722	682
D=30 nm	0.66	-0.018942	683
D=40 nm	0.66	-0.014118	683
D=50 nm	0.66	-0.01125	683
D=60 nm	0.66	-0.009349	683
D=70 nm	0.66	-0.007998	683
D=80 nm	0.66	-0.006987	683
D=90 nm	0.66	-0.006203	683
D=100 nm	0.66	-0,005578	683

TABLE 4.3: The influences of D on equilibrium c_2, minimum ΔG_{total} and GB energy of Pd-Cu alloy

Where, based on the calculations, it is clear that with the increasing of grain size D, the minimum ΔG_{total} will shift towards the positive direction of y-axis. This is

because when D is very large, the volume fraction of grain boundary region would be relatively small, therefore, most of solute atoms may prefer to stay in the bulk region due to the lack of space in GB, therefore there would be only a weak solute segregation to GB region, leading to a small change of Gibbs free energy after segregation. Furthermore, by substituting ΔG_{total} into Eq.3.53, the effective GB energy of Pd-Cu alloy can be obtained. According to the calculations, the solved effective GB energies are close to that of pure Pd, thus we may derive that the segregation of copper may not effectively inhibit the grain growth of $Pd_{0.7}Cu_{0.3}$.

4.3.3 The influences of GB thickness t in Pd-Cu system

The grain boundary thickness t will also affect the volume fractions of bulk region and GB region, in further, it may affect the Gibbs free energy of the alloy system, this is because the total free energy of system that contributed from the bulk and GB regions are weighted by f_{bulk} and f_{gb}. In this case, if $D = 20nm$ and $c_0 = 0.3$, the grain boundary thickness t should be smaller than 2.24 nm, to ensure c_1 as a positive value. Thus, the thickness t will be taken as 0.5 nm, 1 nm, and 2 nm, and the results will be given as follows.

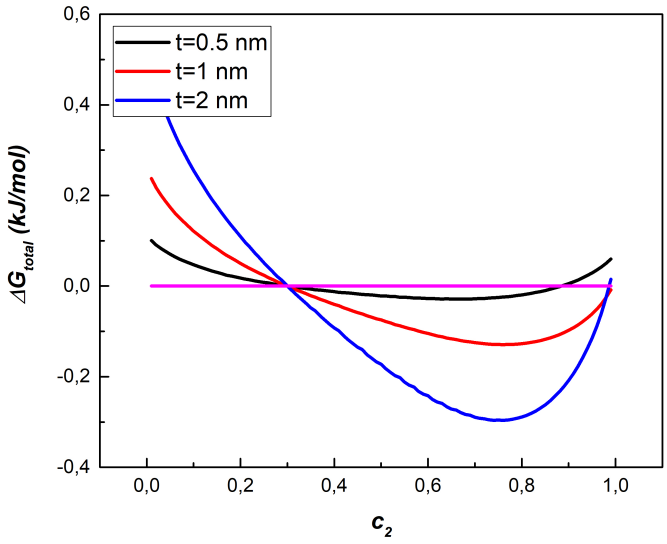

FIGURE 4.4: The ΔG_{total} vs c_2 plots correspond to the different t (Pink line indicates the $\Delta G_{total} = 0$)

Pd-Cu	c_2 (Equilibrium)	ΔG_{total} (kJ/mol)	Effective GB energy (mJ/mol)
t=0.5 nm	0.66	-0.028722	682
t=1 nm	0.76	-0.12912	673
t=2 nm	0.76	-0.296475	634

TABLE 4.4: The influences of t on equilibrium c_2, minimum ΔG_{total} and GB energy of Pd-Cu alloy

Where, based on the above figure, we find the minimum ΔG_{total} keeps decreasing with the increasing of GB thickness t, which will lead to a lower effective grain

boundary energy of $Pd_{0.7}Cu_{0.3}$. These changes can be attributed to the varying of the volume fraction of GB region. When t increases, the volume fraction of GB region will increase accordingly, therefore the energy contributions from GB region $f_{gb}\Delta G_{gb}$ (make a negative contribution to ΔG_{total}) to ΔG_{total}) will dominate the total free energy. If f_{gb} is large, due to the large accommodation space in GB, more solutes will be allowed to enter this region to lower the free energy of system. The influences of thickness t on the solute segregation are much stronger than that of other factors such as D and c_0, which are reflected on the magnitude of minimum ΔG_{total}. In addition, the equilibrium solute concentration c_2 seems not to be affected by the variations of GB thickness t.

4.3.4 The influences of temperature T in Pd-Cu system

Our free energy of mixing of the binary Pd-Cu system contains a configuration entropy term, which is predominantly coupled with temperature T. The most general effect of temperature T is to randomize the solute distribution, and to decrease the tendencies of solute segregation to GB region. When temperature T is high, the entropy of mixing is supposed to exert huge influences on ΔG_{total}. In the following discussion, T will be taken from 400 K up to 1000 K, with a interval of 200 K; $c_0 = 0.3$; $D = 20nm$; $t = 0.5nm$; $m = 5$ for GB region; and $del = 0.5$. The results are given as

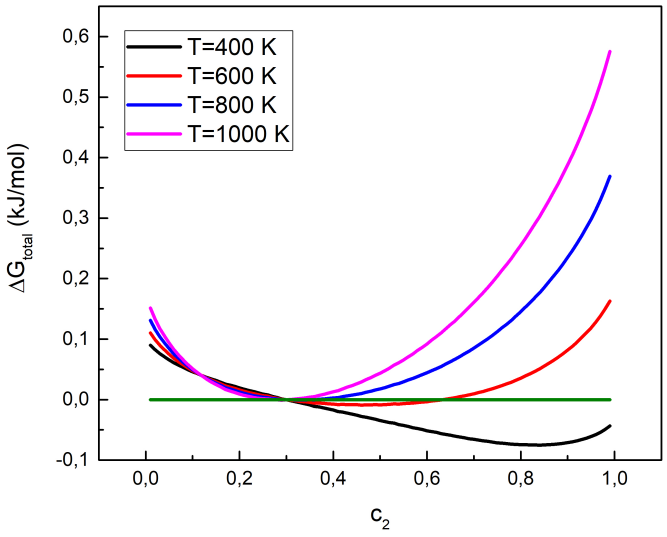

FIGURE 4.5: The ΔG_{total} vs c_2 plots correspond to the different T (Green line indicates the $\Delta G_{total} = 0$)

Pd-Cu	c_2 (Equilibrium)	ΔG_{total} (kJ/mol)	Effective GB energy (mJ/mol)
T=400 K	0.84	-0.075088	680
T=500 K	0.66	-0.028722	682
T=600 K	0.5	-0.008576	683
T=700 K	0.37	-0.002531	683
T=800 K	0.33	-0.000527	683
T=900 K	0.3	0	683
T=1000 K	0.3	0	683

TABLE 4.5: The influences of T on equilibrium c_2, minimum ΔG_{total} and GB energy of Pd-Cu alloy

Where, according to the results, we find with the increasing of temperature T, the minimum ΔG_{total} will increase accordingly, and the equilibrium solute concentration c_2 will shift towards the negative direction of x-axis, which suggests the solute and solvent atoms tend to randomly mix with each others at high temperature, in stead of separating with each others.

4.3.5 The influences of *del* in Pd-Cu system

The introduced parameter *del* indicates the fraction of amorphous phase in grain boundary region, and the variation of *del* can exert influences on the free energy of GB region. Because the energy of GB region contains the contributions both from the amorphous phase and from the solid solution, where the weight of contributions will be determined by the introduced parameter *del*.

Moreover, an amorphous phase is considered to be produced from crystalline phases by two steps: melting the crystalline phase at first, then mixing the molten phases. For binary alloy systems, in general, if the temperature is below their melting temperature, then the free energy of melting term will be always positive [30], therefore, the Gibbs free energy of amorphous phase is thought to be higher than that of solid solution. Hence, if *del* is large, then amorphous phase will occupy the GB region, which may increase the Gibbs free energy of GB region. Whereas if *del* is small, then the dominant of solid solution will decrease the free energy of GB region. In this case, we consider *del* as a variable, which will be chosen as 0, 0.5 or 1. If $del = 0$, the GB region will consist of a complete solid solution; if $del = 0.5$, the GB region will consist of a partial solid solution and a partial amorphous phase; whereas if $del = 1$, GB region will be fully amorphous. As for remained parameters, they will be assigned as: $c_0 = 0.3$; $D = 20nm$; $t = 0.5nm$; $T = 500K$; $m = 5$ (for GB region); and $m = 8$ (for bulk region).

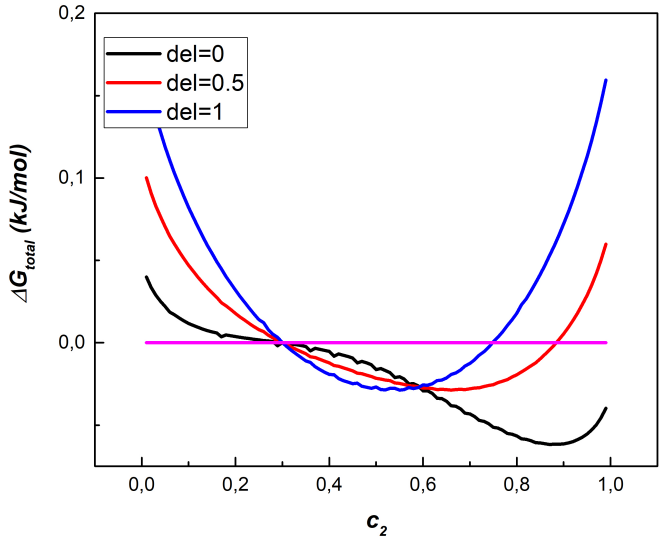

FIGURE 4.6: The ΔG_{total} vs c_2 plots correspond to the different *del* (Pink line indicates the $\Delta G_{total} = 0$)

Pd-Cu	c_2 (Equilibrium)	ΔG_{total} (kJ/mol)	Effective GB energy (mJ/mol)
del=0	0.87	-0.061793	680
del=0.5	0.66	-0.028722	682
del=1	0.55	-0.028694	683

TABLE 4.6: The influences of *del* on equilibrium c_2, mimimum ΔG_{total} and GB energy of Pd-Cu alloy

According to the results, it is clear that when grain boundary region is considered as a complete solid solution ($del = 0$), the solute atoms (Cu) will show a strong segregation to grain boundary sites to reduce the energy of alloy system. Moreover, if we compare the minimum values of ΔG_{total} that corresponding to different *del*, we will find that when $del = 0$, its corresponding minimum ΔG_{total} is the smallest one. Whereas, if $del = 1$, grain boundary region will be fully amorphous, then the solute atoms will show less tendency of segregation. The reason is that the Gibbs free energy of mixing is negative for most of solid solutions, and the mixing term can lower the energy of systems, whereas the amorphous phase will make a positive contribution to the free energy of the binary system, i.e., $H^{top}_{gbc_0}$ and $H^{top}_{gbc_2}$, which could restrain the solute segregation to GB region.

Chapter 5

XRD analysis of thin film samples

In this chapter, X-ray diffraction (XRD) analysis that performed on both the $Pd_{0.7}Cu_{0.3}$ and the pure Pd thin films will be discussed. The reason why we choose Cu 30 wt% of Cu as the initial solute concentration lies in the fact that Pd-Cu tends to form a bcc structure when the solute (Cu) concentration is between 30 and 60 wt%, which may enhance the permeability of H2 [37]. However, if the Cu concentration is taken as 40 wt%, the bcc region of $Pd_{0.6}Cu_{0.4}$ is very narrow and can easily affected during preparation [37]. Based on these reasons, the $Pd_{0.7}Cu_{0.3}$ alloy composition will be selected.

In general, the XRD analysis performed on Pd-Cu and pure Pd thin film samples mainly can be divided into three parts: (1) The full X-ray diffraction patterns of annealed and unannealed samples will be obtained, where we can obtain the samples' phase information, intensities and peak positions of various diffraction peaks. Moreover, if we compare the x-ray pattern of annealed sample with that of the same unannealed sample, we will have a general feeling regarding whether any changes occur in the the XRD pattern, i.e., the shift of diffraction line, the broadening of the diffraction peak, and the formation of second phase. Thus, in order to determine which factors that lead to these changes, the further XRD experiments are needed, including the XRD residual stress measurements and the X-ray peak broadening analysis. (2) The main function of the residual stresses measurements that performed in our study is to measure the alloy composition and to find out whether the solute segregation occurs after the annealing. This can be achieved by applying the so called $\sin^2\Psi$ method that applied to the sample's certain selected diffraction plane. In our study, the (220) diffraction plane is selected for both the Pd-Cu and pure Pd, and the reason of this selection will be given in the next section. Moreover, the residual stresses that remained in the samples will also be determined by applying the XRD residual stress measurements. (3) The X-ray peak broadening analysis aims at measuring the broadening of different diffraction peaks, where the FWHM (full width at half maximum) and the 2θ peak position for different diffraction peaks will be record for both samples. By applying the so-called "USDM" modified WIlliam-Hall method [39], the crystalline size and microstress of samples can be determined, which will help us to identify whether the grain growth occur phenomena occur in samples after the annealing process. It is mentioned that the peak broadening analysis will be performed at both the room temperature and high temperature. As for the high temperature measurement, only the (111) and (200) peaks will be considered, this is because the intensities for other peaks are too weak to be measured.

5.1 The full X-ray diffraction patterns of Pd-Cu and pure Pd thin films

In the full X-ray diffraction patterns, the peak shapes, 2θ peak positions, FWHMs, and the peak intensities will be recorded of the various diffraction peaks, which include the (111), (200), (311) and (222).

5.1.1 Experiment

5.1.1.1 Sample Condition

For $Pd_{0.7}Cu_{0.3}$ thin film, magnetron sputtering technique was used to deposit Pd-Cu thin film with a 30 percent of Cu and 70 percent of Pd on a silicon wafer, which was designed as a columnar structure of thin film with around 80 nm thickness. The original thin film sample on silicon substrate was cut into identical two pieces with each size 18 mm$\times$18 mm. Both of the two pieces were measured reassembly, they are analyzed by XRD at room temperature, then were heated up to 500 K and annealed in D5005 TT at constant temperature, under the protection of nitrogen gas for over 60 hours, during the constant heating procedure, high temperature measurements are performed on (111) and (200) diffraction planes. After the heat treatment, the sample was allowed to cool down to room temperature 300 K naturally and re-measured by XRD, and the full-peak pattern is obtained.

For pure Pd thin film, the sample was prepared in the same way as that of PdCu alloy. Magnetron sputtering technique was used to deposit a 100 % of Pd atoms on a silicon wafer with a columnar structure. The thickness and columnar size of pure Pd thin film are also designed as the same as that of Pd-Cu, and the heat treatment condition will be kept the same as well.

5.1.1.2 Instrument and Parameters

X-ray diffraction was performed on $Pd_{0.7}Cu_{0.3}$ and pure Pd individually by powder X-ray diffraction using BrukerD8 Advance diffractometer with Bragg-Brentano geometry and Lynxeye position sensitive detector, divergence slot V12, scatter screen height 5mm. The power samples were fixed on a Si510 wafer in holder L510. XRD patterns from 10° to 130° 2θ were recorded using Cu Kα1 radiation with wavelength equaling to 0.154 nm. The measurement conditions: tube voltage of 45 kV, tube current of 40 mA, sample spinning, step scan mode with a step size of 0.02° 2θ and counting times per step 2 and 5 s. The instrumental broadening was corrected by using LaB_6 powder. As for the data evaluation, Bruker software DiffracSuite.EVA vs 4.3. Pamalytical Xpert Stress 2.0. were utilized.

5.1.2 Results and discussions

5.1.2.1 The full X-ray diffraction patterns of annealed and unannealed $Pd_{0.7}Cu_{0.3}$

The diffraction from the $Pd_{0.7}Cu_{0.3}$ thin film satisfies the Bragg's law $n\lambda = 2dsin\theta$, where n is an integer, λ is the wavelength of the Cu Kα_1 radiation (0.154 nm), and d is the inetplannar spacing between the same sets of $\{hkl\}$ planes, and θ is the diffraction angle. From the XRD analysis, the plots of diffraction intensity versus the 2θ peak position for the unannealed and annealed sample can be obtained, which is given in the following figure.

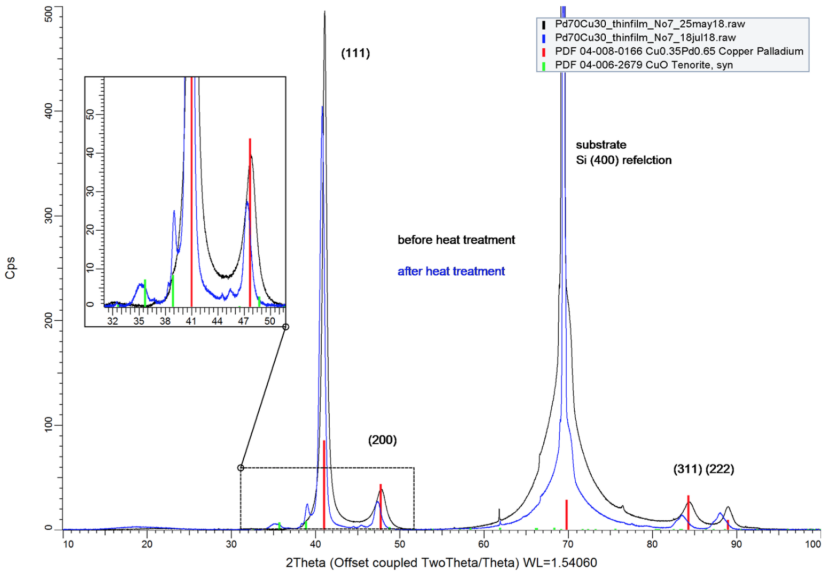

FIGURE 5.1: The full XRD patterns of unannealed and annealed $Pd_{0.7}Cu_{0.3}$ thin film (Annealing temperature: 500 K)

Where, according to the figure, several diffraction peaks of $Pd_{0.7}Cu_{0.3}$ are observed, which correspond to the (111), (200), (311) and (222) diffraction planes. A small peak at 2θ 35° is detected, which implies the formation of CuO, thus we may deduce the oxygen in chamber is not fully evacuated, and some still remained in the nitrogen environment. No extra peaks that correspond to the second-phase precipitates were detected. It is observed that the intensities of the Bragg peaks of annealed Pd-Cu thin film were decreased when compared with that of measured before the heat treatment. The clear peak shifts are observed in (200), (311) and (222) diffraction planes. Moreover, we may expect that there exists the the peak narrowing effect. These changes in Bragg peaks could be attributed to the influences of lattice strain (including the macrostrain and microstrain) and crystallite size [39]. Thus, further X-ray investigations are needed, in order to separate the contributions from different factors, where we can determine whether the solute segregation occurs in $Pd_{0.7}Cu_{0.3}$ binary alloy, and whether the grain growths occur in both the Pd-Cu and pure Pd thin films.

5.1.2.2 The full X-ray diffraction patterns of annealed and unannealed pure Pd

Based on the XRD analysis that performed on pure Pd, the full XRD patterns of unannealed and annealed Pd are given as

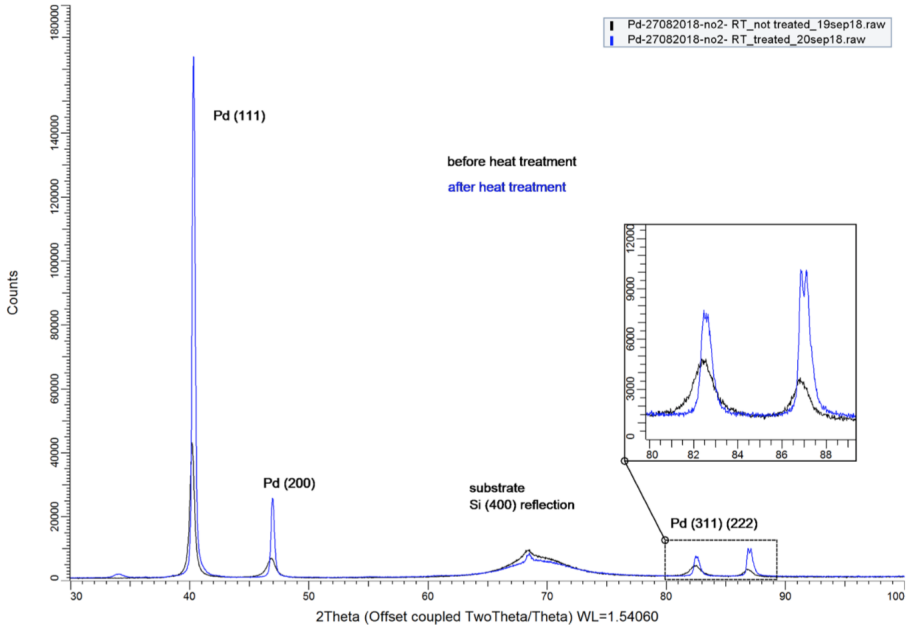

FIGURE 5.2: XRD pattern of unannealed and annealed Pd thin film (Annealing temperature: 500 K)

Where, according to this figure, (111), (200), (311) and (222) four diffraction planes are observed. And a small peak at 2θ 34° is detected, which implies the formation of PdO, again, we may deduce the oxygen is not fully evacuated in the nitrogen environment. It is mentioned that the intensities of the Bragg peaks of annealed Pd thin film were strongly increased when compared with the intensities of unannealed sample. No extra peaks that correspond to the second-phase precipitates were detected. A clear peak shift is observed in (222) diffraction plane. Moreover, the peak broadening effect is very obvious in (200), (111) and (222) planes. Thus, the further X-ray residual stress measurement and peak broadening analysis are needed.

5.2 XRD residual stress measurements of Pd-Cu and pure Pd thin films

5.2.1 Introduction

X-ray diffraction can be utilized to measure the residual stresses that remained in solid samples. When sample is strained, elongations and contractions are generated within the crystal lattice, which can change the interplanar spacing of $\{hkl\}$ lattice planes. This introduced macrostrains will lead to a shift of the diffraction lines to new 2θ positions [40]. The XRD residual stress measurement is also called as $sin^2\Psi$ method [41], it relies on measuring the shift of the 2θ diffraction peak position for the various Ψ angles. Based on the method, a specific diffraction plane is selected and the interplanar distances between the same set of (hkl) planes are measured from a coupled θ-2θ scan under the different tilt Ψ angle. Where Ψ denotes the angle between the diffracting plane normal and the sample surface normal. By plotting the the interplanar distance d-spacing with respect to the $\sin^2\Psi$, the important parameters: macrostress, macrostrain and lattice constant of the selected lattice plane can be determined.

In this section, XRD residual stress measurements are performed on both Pd-Cu and pure Pd thin films before and after the heat treatment. The purpose of these experiments lies in the two facts: (1) strain-free lattice parameter can be determined from the experiments. For $Pd_{0.7}Cu_{0.3}$ alloy, by using the solute (solvent)-weighted average approach (the Vegard's law), the measured no strain lattice parameter a_0 can be associated with the concentrations of alloy constituents, thus the alloy composition can be obtained. If we compare the alloy compositions of Pd-Cu thin film measured before and after the heat treatment, therefore, the degree of solute segregation could be determined. For pure Pd, we expect the strain-free lattice parameter will not be changed after the annealing. The shift of diffraction line is only attributed to the influences of macrostresss and the crystallite size, without any influences from the segregation-introduced stresses. (2) Macrostresses (macrostrains) will also be solved from the slope of linear d-spacing vs $sin^2\Psi$ plot, and these stresses can make contributions to the peak shift. In this XRD residual stress measurements, a high-2θ diffraction peak (220) is selected for both the Pd-Cu and pure Pd thin films, to ensure a higher sensitivity to strain. This is because the higher 2θ peaks have much lower intensities and irregular shapes, which are not accessible or are too weak for accurate measurements [41].

5.2.2 Experimental condition

5.2.2.1 Sample condition

For Pd-Cu thin film, magnetron sputtering technique was used to deposit Pd-Cu alloy with a 30 wt% of Cu and 70 wt% of Pd on a silicon wafer, which was designed as a columnar structure of thin film with around 80 nm thickness. The thin film sample on silicon substrate, 18*18mm, is labeled as $Pd_{0.7}Cu_{0.3}$, and they will be cut into two pieces (9×18 mm) for the heat treatment. These residual stress measurements are performed before and after heat treatment. The annealing condition is given as: long time heating at 500 K for over 60 hours, in D5005 TT, under the protection of nitrogen gas. Moreover, because the sample films are deposited while spinning, the possibly present residual stress would be rotational symmetric, therefore it is sufficient to perform the $\theta - 2\theta$ scans at various Ψ angles in an arbitrary ϕ direction.

For pure Pd thin film, it is considered as the reference group. The same magnetron sputtering technique was used to deposit a 100 % of Pd atoms on a silicon wafer with a columnar structure 20 nm. Both the thickness and columnar size of pure Pd thin film are designed as the same values as that of Pd-Cu alloy. And the sample on silicon substrate 18*18mm, labeled as: "pure Pd". Before doing the heat treatment, Pd sample will be cut into two pieces beforehand. The annealing experiments will be performed at the following condition: long time heating at 500 K for over 60 hours, in D5005 TT, under the protection of nitrogen gas.

5.2.2.2 Instrument and Parameters

In XRD residual stress measurements, the $\sin^2\Psi$ method was applied on sample's (220) diffraction plane before and after the heat treatment. Pd-Cu thin film was mounted on a Si510 wafer in holder L510, where the film tilted angle Ψ ranged from 18° to 45° with step size 0.03°, for each Ψ, the corresponding interplanar distance d was recorded. All the scans were carried out by using the Bruker D8 Discover with Eulerian cradle diffractometer. And the size of the incident beam-defining collimating slit was set as: divergence 0.35°, height 4 mm, width 4mm, whereas the size

of the diffracted beam-defining parallel sollerslit was set as: 0.35°. And the x-ray diffraction analysis was performed by using Co Kα radiation, under the operation voltage and current equaling to 45 kV and 25 mA accordingly. The measured data was evaluated by using DiffracSuite.EVA vs 4.3.Pamalytical Xpert Stress 2.0, which generated the partial XRD patterns of (220) peak that corresponding to different Ψ angles, and a modified Lorentzian method was used to fit the diffraction peak. Then, by analyzing these XRD patterns, some important outputs can be generated including the interplanar distances, FWHM (half the maximum intensity) and the 2θ peak positions, which are denoted in the following table.

5.2.3 Results and analysis

5.2.3.1 The XRD $\theta - 2\theta$ patterns of the (220) reflection of $Pd_{0.7}Cu_{0.3}$ thin film before and after the heat treatment

The XRD $\theta - 2\theta$ pattern of the (220) lattice plane of Pd-Cu thin film was measured under the different Ψ angles. As for each Ψ angle, a full scan of (220) plane was completed. The XRD pattern of (220) planes before and after heat treatment are given as

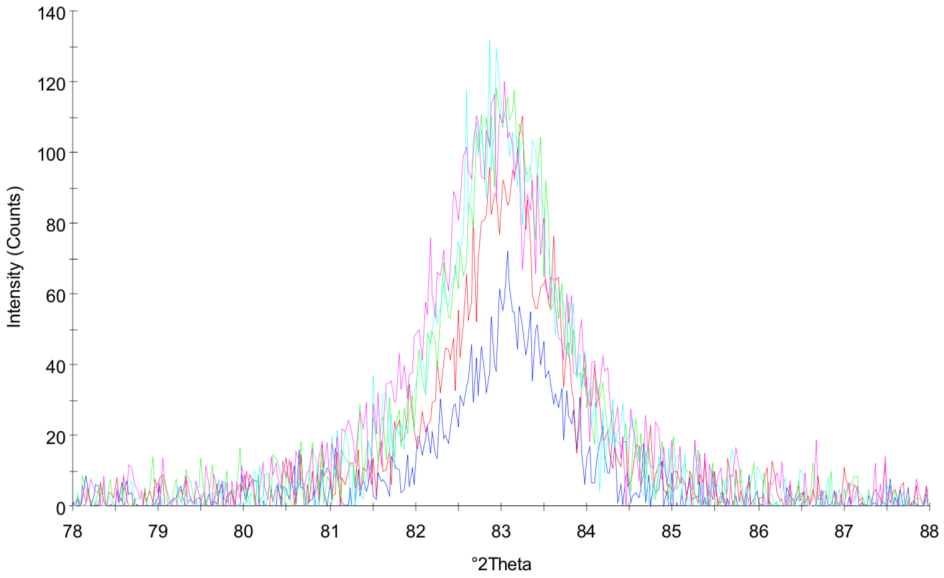

FIGURE 5.3: The XRD pattern of the (220) reflection of unannealed $Pd_{0.7}Cu_{0.3}$ thin film

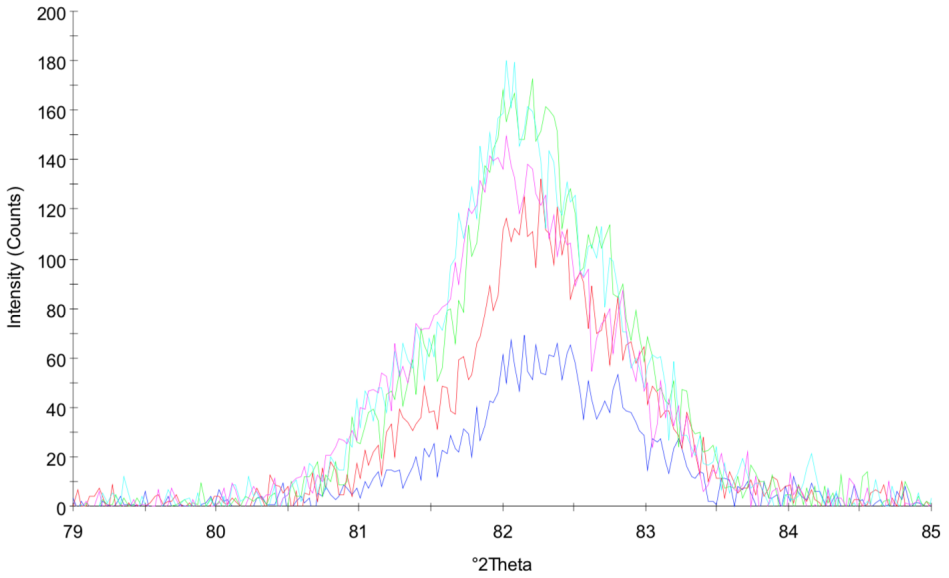

FIGURE 5.4: The XRD pattern of the (220) reflection of annealed $Pd_{0.7}Cu_{0.3}$ thin film

Where, the upper one denotes the XRD pattern of Pd-Cu alloy measured before the heat treatment, whereas the lower one denotes the XRD pattern measured after the heat treatment. In these plots, x-axis represents 2θ peak position and y-axis represents the intensity of diffracted beam. The various colorful fitting lines are corresponding to different Ψ angles. If we compare these two figures, it is obvious that the maximum peak intensity has changed after the heat treatment. In addition, a clear peak shift about 0.7° is observed, which could be resulted from the composition change or the influences of macrostress. Based on these XRD patterns, data analysis will be performed by applying the Pamalytical Xpert stress software, which will generate the following outputs: 2θ peak position, interplanar distance d, Ψ angle, and FWHM.

Scan Pd-Cu thin film	Peak position ($2\theta^\circ$)	$\Psi(^\circ)$	$sin^2\Psi$	d-spacing (nm)	FWHM ($2\theta^\circ$)
1	83.0681	18.43	0.1	0.13490	1.065
2	83.0761	26.57	0.2	0.13489	1.291
3	83.0223	33.21	0.3	0.13496	1.307
4	82.9976	39.23	0.4	0.13500	1.272
5	82.9188	45	0.5	0.13510	1.606

TABLE 5.1: The outputs of XRD pattern of the (220) reflection of unannealed Pd-Cu thin film

Scan Pd-Cu thin film	Peak position ($2\theta^{\circ}$)	$\Psi(^{\circ})$	$sin^2\Psi$	d-spacing (nm)	FWHM ($2\theta^{\circ}$)
1	83.0681	18.43	0.1	0.13592	1.078
2	83.0761	26.57	0.2	0.13596	1.154
3	83.0223	33.21	0.3	0.13604	1.163
4	82.9976	39.23	0.4	0.13614	1.187
5	82.9188	45	0.5	0.13622	1.254

TABLE 5.2: The outputs of XRD pattern of the (220) reflection of annealed Pd-Cu

5.2.3.2 d-spacing vs $\sin^2\Psi$ plots of Pd-Cu thin film sample

The purpose of plotting the numerical values of interplanar distances d as a function of $\sin^2\Psi$ is to solve the strain-free lattice parameter a_0 from stain-free distance d_0 (a_0=$d_0\sqrt{k^2+h^2+l^2}$). In the meantime, after removing all the external forces, the residual stress (strain) remained in the sample also can be determined from this plot, where the slope of the linear fitting curve indicates the numerical value of macrostress. The principles of deriving a_0 and macrostress are given as follows. An isotropic material is subjected to a pure tension that a normal stress acts only in a single direction, however in general, there will be stress components acting in two or three directions at right angles to one another, forming the so-called biaxial or triaxial systems. If we assume a plane stress condition $\sigma_{33} = 0$, then the strain can be expressed as

$$\frac{d_{\Phi\Psi} - d_0}{d_0} = \frac{1+\nu}{E}\sigma_{\Phi} sin^2\Psi - \frac{\nu}{E}(\sigma_{11} + \sigma_{22}) \tag{5.1}$$

However, in this experiments, both Pd and Pd-Cu alloy are the anisotropic materials, which means their properties are dependent on directions. Therefore, the elastic constant E that used for isotropic material should be modified into the (hkl)-dependent E_{hkl}, which relies on the different diffraction planes. In Panalytical Xpert Stress software, the X-ray elastic constants s_1 and $\frac{1}{2}s_2$ (with unit TPa^{-1}) are utilized in the stress analysis, which are defined by being associated with the elastic constant E_{hkl}, the Poisson's ratio ν. The expressions are given as

$$s_1 = \frac{-\nu}{E_{hkl}} \tag{5.2}$$

$$\frac{1}{2}s_2 = \frac{1+\nu}{E_{hkl}} \tag{5.3}$$

Therefore, Eq.5.1 can be rewritten as

$$\frac{d_{\Phi\Psi} - d_0}{d_0} = \frac{1}{2}s_2\sigma_{\Phi} sin^2\Psi + s_1(\sigma_{11} + \sigma_{22}) \tag{5.4}$$

Where, in above equations, ν denotes the Poisson's ratio of the alloying element, for Pd, it is equal to 0.39; E_{220} denotes the elastic constant of (220) plane, which equals to 0.1355 TPa; σ_{11} and σ_{22} denote the stresses acting on the first and second principal directions individually. Due to the rotational symmetric property, the biaxial stress can be written as

$$\sigma_{\Phi} = \sigma_{11}cos^2\Phi + \sigma_{22}sin^2\Phi \tag{5.5}$$

Moreover, because thin film sample was deposited while spinning, the possibly present residual stress would be rotational and symmetric, therefore we have σ_{11}=σ_{22}, if we substitute this equation into Eq.5.5, σ_{11}=σ_{22}=σ will be obtained. On the basis of these assumptions, if we assume a no strain condition (ϵ=$\frac{d_{\Phi\Psi}-d_0}{d_0}$=0), the following equation could be derived as

$$sin^2\Psi_0 = \frac{-s_1(\sigma_{11}+\sigma_{22})}{\frac{1}{2}s_1\sigma_\Phi} = \frac{-2s_1}{\frac{1}{2}s_2} = 0.561 \tag{5.6}$$

Where, by utilizing the condition that $sin^2\Psi_0 = 0.561$, the strain-free interplanar distance d_0 can be directly determined from the d-spacing vs $sin^2\Psi$ plots, in further step, the strain-free lattice parameter can be determined from d_0 by $a_0 = d_0\sqrt{h^2+l^2+k^2}$.

Before the heat treatment, we can make a d-spacing vs $sin^2\Psi$ plot of $Pd_{0.7}Cu_{0.3}$ sample by using the data provided in TABLE 5.1, and the figure is given as

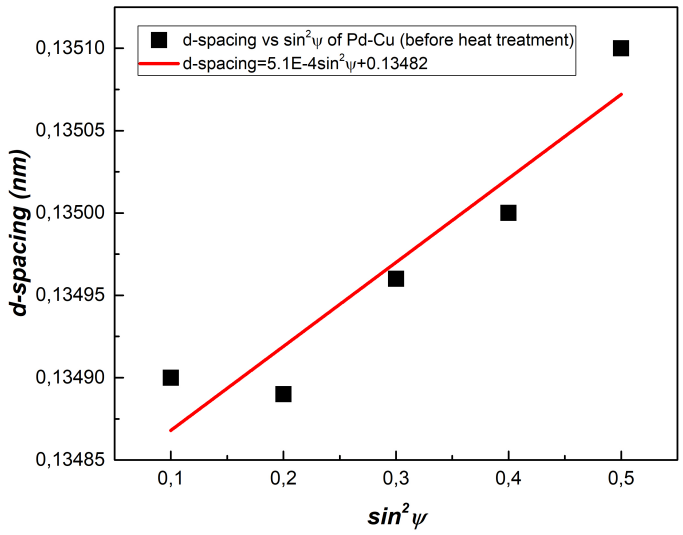

FIGURE 5.5: The d-spacing vs $sin^2\Psi$ plot of (220) plane of $Pd_{0.7}Cu_{0.3}$ measured before heat treatment

Where, in this plot, x-axis denotes $sin^2\Psi$ and y-axis denotes the numerical values of d-spacing. It is obvious that the fitted curve satisfies a linear behaviour, and the regression equation can be solved as

$$d - spacing = 5.1E - 4sin^2\Psi + 0.13482 \tag{5.7}$$

Where, the slope of the trend line is 5.1E-4, with a correlation (R) factor equaling to 0.95. If we substitute $sin^2\Psi_0$=0.561 into this equation, d_0 can be determined, which is equal to 0.13511 nm, and it is corresponding to the interplanar distance between the same set of planes without any external stress. Furthermore, the strain-free lattice parameter a_0 of (220) plane of Pd-Cu alloy system can be determined from

$$a_0 = d_0\sqrt{h^2+k^2+l^2} = d_0\sqrt{8} = 0.3821\ nm \tag{5.8}$$

The solved a_0 can be associated with the alloy composition via the Vegard's law, where the lattice constant of an alloy is approximately equal to the rule of mixtures of individual lattice parameter of this alloying constituents that measured at same temperature. For example, if we assume a binary alloy with a given composition of $A_{c_0}B_{1-c_0}$, where A denotes the solute atoms (Cu) with a solute concentration of c_0, and B denotes the solvent atoms (Pd) with a solvent concentration of $1 - c_0$, then the lattice parameter of solid solution $A_{c_0}B_{1-c_0}$ could be represented as

$$a_{A_{c_0}B_{1-c_0}} = c_0 a_A + (1 - c_0)a_B \tag{5.9}$$

Thus, by rearranging the formula above, the solute (A) concentration can be resolved as

$$c_0 = \frac{a_{A_{c_0}B_{1-c_0}} - a_B}{a_A - a_B} \tag{5.10}$$

Where, in this experiment, for Pd-Cu alloy, a_A and a_B denote the lattice constants of Cu and Pd separately. Based on the reference [42], we find a_{Cu}=0.36149 nm and a_{Pd}=0.38907 nm, by combing the measured lattice parameter of alloy $A_{c_0}B_{1-c_0}$ a_0=0.3821 nm, we are able to determine the initial solute concentration of Cu atoms before the heat treatment via Eq.5.10, which is equal to 0.253, thus the corresponding alloy composition will be $Pd_{0.75}Cu_{0.25}$.

After the heat treatment, again, by employing the same analyzing approach, we will plot d-spacing with respect to the $sin^2\Psi$, which generates the following results

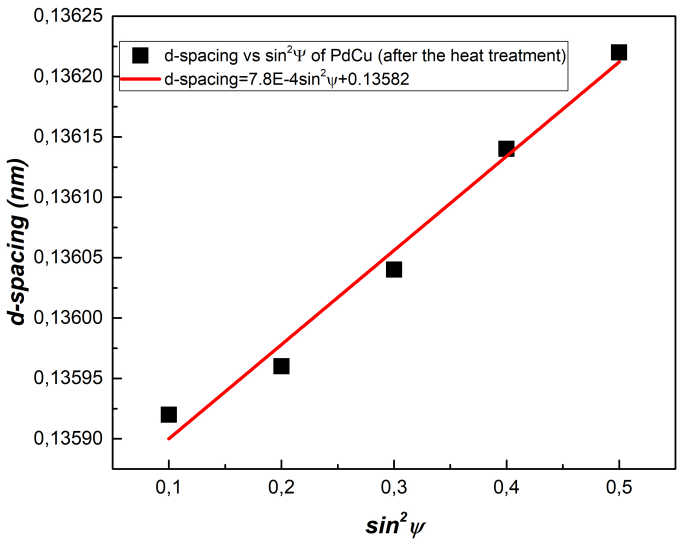

FIGURE 5.6: The d-spacing vs $sin^2\Psi$ plot of (220) plane of $Pd_{0.7}Cu_{0.3}$ measured after heat treatment

Where, the fitted curve also shows a linear behaviour as that measured before the heat treatment, and the regression formula is given as

$$d - spacing = 7.8E - 4sin^2\Psi + 0.13582 \tag{5.11}$$

Because we discussed $sin^2\Psi$=0.561, by substituting it into equation, we obtain d_0 as 0.13626 nm. After the heat treatment, the strain-free lattice parameter could be given

as

$$a_0 = d_0\sqrt{h^2 + k^2 + l^2} = d_0\sqrt{8} = 0.3854\ nm \tag{5.12}$$

Furthermore, according to Eq.510, the solute (Cu) concentration of Pd-Cu thin film after annealing is solved as 0.133, which reflects that 13.3% of solute atoms prefer to stay in bulk interior after the heat treatment.

Therefore, when compared the alloy composition of bulk region that measured before the heat treatment, $Pd_{0.75}Cu_{0.25}$, with that of composition measured after the heat treatment, $Pd_{0.87}Cu_{0.13}$, we find the solute concentration of bulk region decreased from 0.25 into 0.13 after annealing, which suggests the change in measured lattice parameters is attributed to the occurrence of solute segregation. However, we are not sure the specific type of solute segregation, whether it is the surface segregation or the GB segregation. Therefore, further studies are recommended, such as TEM technique. Furthermore, in order to verify the rationality of measured lattice parameters of Pd-Cu sample, and to verify whether it is feasible to determine the alloying parameters by using Vegard's law, then we will compare the calculated a_0 with the values provided in literature. According to the reference [43], for a palladium copper alloy, there exists a linear relationship between the alloy's lattice parameter and the solute (Cu) concentration. The data are displayed in the following table, which were measured at 298 K.

Pd-Cu (T=298 K)	Lattice constant (nm)	Solute concentration (%)
	81.3344	18.43
	81.2922	26.57
	81.2466	33.21
	81.1981	39.23
	81.1586	45

TABLE 5.3: Lattice parameters of Pd-Cu from reference reference paper [43]

Based on the values provided in the above table, if we plot the solute concentration of Cu with respect to the corresponding lattice parameter, then we will obtain

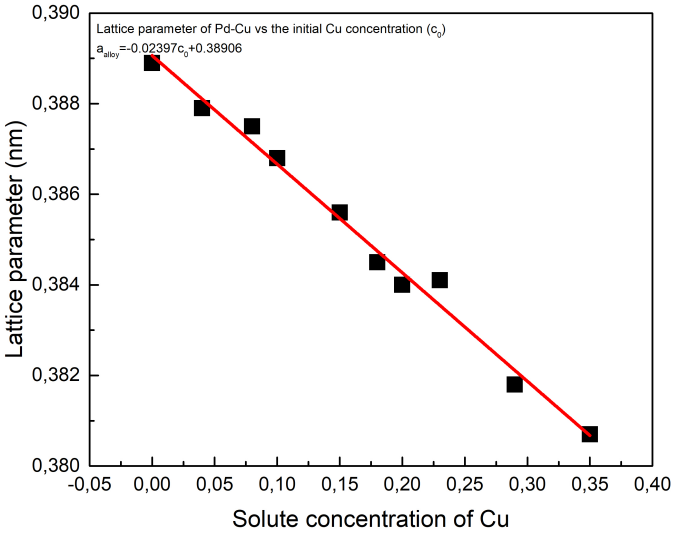

FIGURE 5.7: The relationship between the alloy's lattice parameter and the solute (Cu) concentration from reference

Where, the fitted curve shows a linear behavior between the two variables, which reflects the feasibility of using Vegard's law in our case, to estimate the lattice parameter of Pd-Cu thin film.

5.2.3.3 Residual stress and strain of sample $Pd_{0.7}Cu_{0.3}$

The residual stresses remained in the sample can be determined from the slope of the linear fitted curve of d-spacing vs $\sin^2\Psi$ plot. This is because we can rewrite Eq.5.4 into the following form

$$d_{\Phi\Psi} = \frac{1}{2}s_2\sigma_\Phi d_0 sin^2\Psi + s_1 d_0(\sigma_{11} + \sigma_{22}) + d_0 \tag{5.13}$$

From the above equation, it is clear the slope of the tread line is equal to $\frac{1}{2}s_2\sigma_\Phi d_0$, therefore, if d_0 and slope are provided, σ can be directly calculated by

$$\sigma = \frac{slope}{\frac{1}{2}s_2 d_0} \tag{5.14}$$

In addition, because sample was subjected to a uniaxial loading, if the remained residual stresses are assumed to be small, then Hook's law can be employed to estimate the numerical value of macrostrain, which is given as

$$\epsilon = \frac{\sigma}{E_{hkl}} \tag{5.15}$$

Therefore, after the calculation, residual stresses and strains remained in the system before and after the heat treatment can be given as

Pd-Cu	Residual stress (MPa)	Residual strain (ppm)
Before the heat treatment	358±76	3717±791
After the heat treatment	547±44	4674±503

TABLE 5.4: Residual stress and strain remained in Pd-Cu thin film

Where, according to the calculation results, we find the residual stress (strain) has increased after the annealing procedure. The amount of increased residual stresses is equal to $\Delta\sigma = \sigma_{after} - \sigma_{before} \approx 189MPa$, which could be attributed to these factors: the solute segregation of Cu, the stresses introduced during the deposition procedure, and the influences of thermal heating.
In the meantime, because the sample was subjected to the heat treatment that heated from room temperature 300 K up to 500 K, and retaining for more than 60 hours, later it was cooled reversely to the room temperature. The change in temperature can lead to the internal thermal expansions between different materials with the distinct thermal coefficients. The thermal coefficients of Pd, Cu and Si are given as $\alpha_{Pd} = 1.18 \times 10^{-5}\ K^{-1}$, $\alpha_{Cu} = 1.65 \times 10^{-5}\ K^{-1}$ and $\alpha_{Si} = 2.6 \times 10^{-6}\ K^{-1}$ accordingly [42], therefore the thermal stresses may exist between Pd and Si wafer, and between Cu and Pd elements (when solute segregation occurs). The magnitude of thermal stresses can be roughly estimated by using the following equation

$$\sigma_{thermal} = \frac{E_{hkl}}{1-\nu}\Delta\alpha\Delta T \tag{5.16}$$

Where, E_{hkl}=0.1355 denotes the elastic constant of (220) plane of Pd; ν=0.39 denotes the Poisson's ratio of Pd; $\Delta\alpha$ denotes the difference of thermal coefficients between two constituents; and ΔT denotes the change in temperature during the heat treatment.

(1) When sample was heated from 300 K up to 500K
The introduced thermal stress between Pd and Si substrate is equal to

$$\sigma_{thermal} = \frac{E_{220}}{1-\nu_{Pd}}(\alpha_{Pd} - \alpha_{Si})(500K - 300K) = 409\ MPa \tag{5.17}$$

The thermal stress between Pd and Cu is equal to

$$\sigma_{thermal} = \frac{E_{220}}{1-\nu_{Pd}}(\alpha_{Cu} - \alpha_{Pd})(500K - 300K) = 209\ MPa \tag{5.18}$$

(2) When sample was cooled down from 500 K to 300K
Now, the thermal stress between Pd and Si substrate is changed into

$$\sigma_{thermal} = \frac{E_{220}}{1-\nu_{Pd}}(\alpha_{Pd} - \alpha_{Si})(300K - 500K) = -409\ MPa \tag{5.19}$$

The thermal stress between Pd and Cu is equal to

$$\sigma_{thermal} = \frac{E_{220}}{1-\nu_{Pd}}(\alpha_{Cu} - \alpha_{Pd})(300K - 500K) = -209\ MPa \tag{5.20}$$

Where, the numerical value of thermal stress between Pd and Cu (209 MPa) is close

to the change of residual stresses (189 MPa) measured before and after the heat treatment, which may suggest the occurrence of Cu segregation, and the change in residual stresses of Pd-Cu system can be attributed to the internal thermal stresses between Pd and Cu that stem from the segregation of copper. Moreover, a part of thermal stresses (i.e., the thermal stress between Pd and Si) may be eliminated by relaxation.

5.2.3.4 The XRD $\theta - 2\theta$ patterns of the (220) reflection of pure Pd thin film before and after the heat treatment

The XRD $\theta - 2\theta$ patterns of (220) diffraction plane of pure Pd sample before and after the heat treatment were also measured under the various Ψ angles, and the following data can be obtained, which includes the 2θ peak position, interplanar distance d, Ψ angle, and FWHM. The XRD patterns of pure Pd are given as

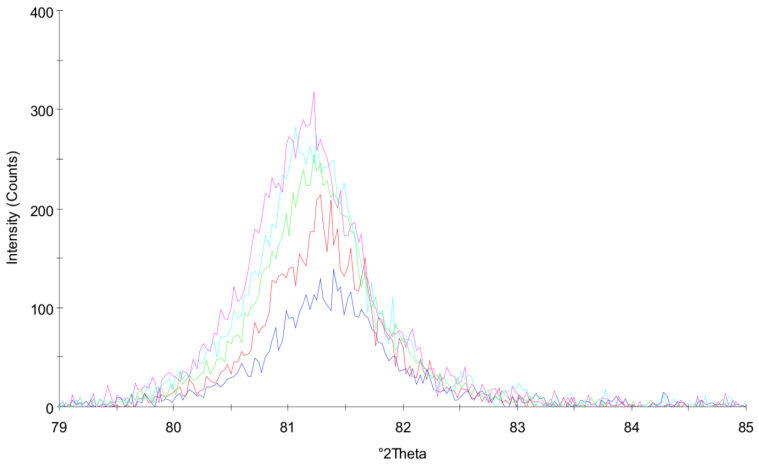

FIGURE 5.8: The XRD pattern of the (220) reflection of unannealed pure Pd thin film

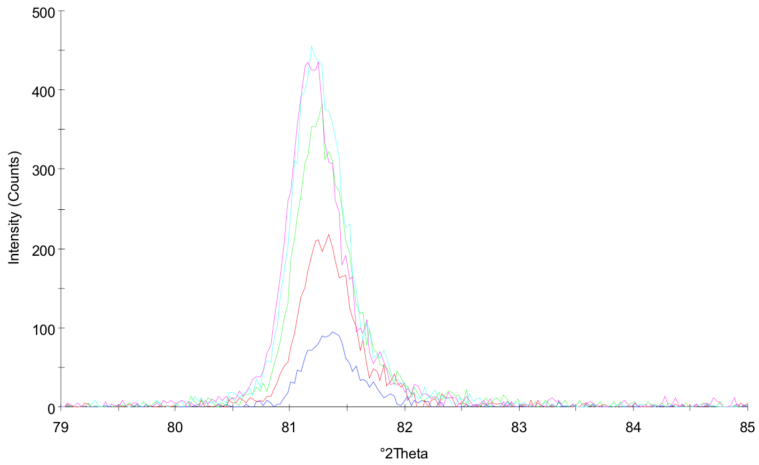

FIGURE 5.9: The XRD pattern of the (220) reflection of annealed pure Pd thin film

Scan Pd thin film	Peak position ($2\theta^{\circ}$)	$\Psi(^{\circ})$	$sin^2\Psi$	d-spacing (nm)	FWHM ($2\theta^{\circ}$)
1	81.3344	18.43	0.1	0.137262	0.958
2	81.2922	26.57	0.2	0.137321	0.945
3	81.2466	33.21	0.3	0.137384	0.973
4	81.1981	39.23	0.4	0.137452	0.964
5	81.1586	45	0.5	0.137507	1.012

TABLE 5.5: The outputs of XRD pattern of the (220) reflection of unannealed Pd thin film

Scan Pd thin film	Peak position ($2\theta^{\circ}$)	$\Psi(^{\circ})$	$sin^2\Psi$	d-spacing (nm)	FWHM ($2\theta^{\circ}$)
1	81.3682	18.43	0.1	0.137215	0.360
2	81.3270	26.57	0.2	0.137272	0.436
3	81.2985	33.21	0.3	0.137312	0.442
4	81.2623	39.23	0.4	0.137362	0.462
5	81.2242	45	0.5	0.137415	0.457

TABLE 5.6: The outputs of XRD pattern of the (220) reflection of annealed Pd thin film

Where, according to these figures, we find there is no obvious change in the peak intensity measured before and after the heat treatment. However, a clear peak shift (0.7°) towards the higher 2θ peak position is observed in the XRD pattern, which could be attributed to the influences of macrostresses remained in the pure Pd thin film.

5.2.3.5 d-spacing vs $sin^2\Psi$ plots of pure Pd thin film sample

Before the heat treatment, we can make a d-spacing vs $sin^2\Psi$ plot of Pd by using the data provided in TABLE 5.4, which generates the following figure

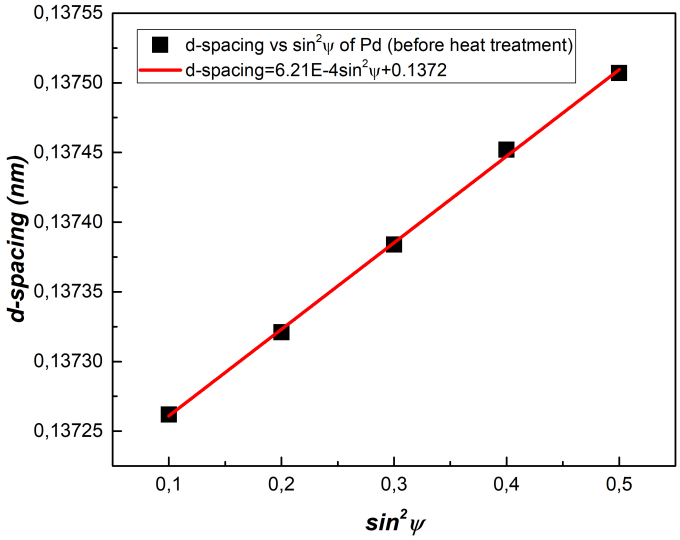

FIGURE 5.10: The d-spacing vs $sin^2\Psi$ plot of (220) plane of pure Pd measured before heat treatment

Where, in this plot, x-axis denotes $sin^2\Psi$ and y-axis denotes the numerical values of d-spacing. It is obvious that the fitted curve also satisfies a linear behaviour as that of Pd-Cu alloy, and fits the data well. The regression equation is solved as

$$d - spacing = 6.21E - 4sin^2\Psi + 0.1372 \tag{5.21}$$

Where, the slope of the trend line is equal to 6.21E-4. If we substitute $\sin^2\Psi_0$=0.561 into this equation, d_0 can be determined, which is equal to 0.1375 nm, and corresponds to the interplanar distance without any external stresses. Furthermore, the strain-free lattice parameter a_0 of the (220) lattice plane of Pd can be determined from

$$a_0 = d_0\sqrt{h^2 + k^2 + l^2} = d_0\sqrt{8} = 0.3889\ nm \tag{5.22}$$

After the heat treatment, again, we employ the same analyzing approach and plot d-spacing with respect to the $sin^2\Psi$

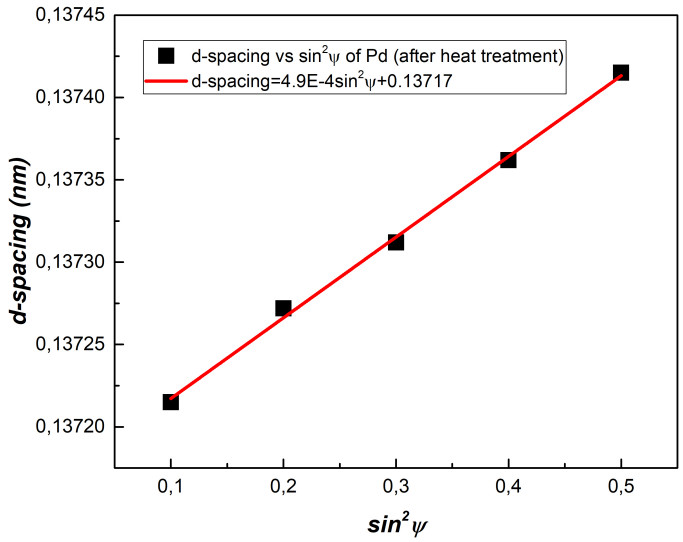

FIGURE 5.11: The d-spacing vs $sin^2\Psi$ plot of (220) plane of pure Pd measured after heat treatment

Where, the fitted curve shows a linear behaviour, and the regression formula is given as

$$d - spacing = 4.9E - 4sin^2\Psi + 0.13717 \tag{5.23}$$

By utilizing $sin^2\Psi$=0.561, we can determine d_0 as 0.1374 nm. After the heat treatment, the strain-free lattice parameter could be given as

$$a_0 = d_0\sqrt{h^2 + k^2 + l^2} = d_0\sqrt{8} = 0.3888\ nm \tag{5.24}$$

Therefore, after comparing the no-strain lattice constants of pure Pd before and after the heat treatment, we find the lattice parameter almost kept unchanged during the annealing procedure, which is agreed with our expectation.

5.2.3.6 Residual stress and strain of pure Pd thin film

The residual stresses remained in the sample Pd can be determined from the slope of the linear fitting curve of d-spacing vs $sin^2\Psi$ plot, which follows the same analyzing method as that of Pd-Cu alloy. Thus the macrostress of Pd will be given as

$$\sigma = \frac{slope}{\frac{1}{2}s_2 d_0} \tag{5.25}$$

In addition, because sample was subjected to a uniaxial loading, if residual strains were assumed to be small, then Hook's law can be employed to estimate the numerical value of strain. The expression of strain is given as

$$\epsilon = \frac{\sigma}{E_{hkl}} \tag{5.26}$$

Therefore, after the calculation, the remained residual stresses and strains of Pd system before and after the heat treatment can be given as

Pd	Residual stress (MPa)	Residual strain (ppm)
Before the heat treatment	437±8	4533±78
After the heat treatment	346±10	3583±103

TABLE 5.7: Residual stress and strain remained in Pd thin film before and after annealing

Where, based on these calculation results, we find both the residual stress and strain of pure Pd were decreased after annealing, which may be attributed to the stress relaxation processes, i.e., by atom diffusion, the rearrangement of lattice structure, or by the generation of dislocations. And the amount of reduced residual stresses is equal to

$$\Delta\sigma = \sigma_{after} - \sigma_{before} \approx -91MPa \tag{5.27}$$

In the meantime, the sample Pd was subjected to a heat treatment, where it was heated from the room temperature up to 500 K and retained for more than 60 hours, then it was cooled back to the room temperature. The change in temperature could lead to internal thermal expansions between Pd thin film and Si wafer. For example, the thermal coefficients of Pd, Cu and Si are $\alpha_{Pd} = 1.18 \times 10^{-5}\ K^{-1}$ and $\alpha_{Si} = 2.6 \times 10^{-6}\ K^{-1}$ accordingly, therefore, thermal stresses may exist between Pd and Si wafer. The thermal stress can be roughly estimated by using the following equation

$$\sigma_{thermal} = \frac{E_{hkl}}{1-\nu}\Delta\alpha\Delta T \tag{5.28}$$

Where, E_{hkl}=0.1355 denotes the elastic constant of (220) plane of Pd; ν=0.39 denotes the Poisson's ratio of Pd; $\Delta\alpha$ denotes the difference of thermal coefficients between two constituents; and ΔT denotes the change in temperature during the heat treatment.

(1) When sample was heated from 300 K up to 500K
The introduced thermal stress between Pd and Si substrate is equal to

$$\sigma_{thermal} = \frac{E_{220}}{1-\nu_{Pd}}(\alpha_{Pd} - \alpha_{Si})(500K - 300K) = 409\ MPa \tag{5.29}$$

(2) When sample was cooled down from 500 K to 300K
Now, the thermal stress between Pd and Si substrate is changed into

$$\sigma_{thermal} = \frac{E_{220}}{1-\nu_{Pd}}(\alpha_{Pd} - \alpha_{Si})(300K - 500K) = -409\ MPa \tag{5.30}$$

Where, according to the calculations, we find the residual stress remained in Pd system is partially relived after the heat treatment ($\Delta\sigma = -91MPa$). In the meantime, the magnitude of thermal stress is much greater than $\Delta\sigma$, which may exert influences on the residual stress remained in the Pd system. Furthermore, the shift of peak position of (220) diffraction plane could be attributed to the influences of the remained residual stresses.

5.3 X-ray peak broadening analysis of Pd-Cu and pure Pd thin films

5.3.1 Introduction

X-ray diffraction technique can provide a great deal of information about the structure of a polycrystalline aggregate. In this study, both $Pd_{0.7}Cu_{0.3}$ and pure Pd thin film were individually annealed at 500 K for over 60 hours. X-ray peak broadening analysis can be utilized to investigate the developments of crystallite in the nanostructured Pd-Cu and Pd thin films after the heat treatment, which aims to investigate whether the grain growth phenomena would occur.

The two main properties extracted from peak width analysis are the crystallite size and lattice strain, whereas the instrumental effect can also play a role in broadening the line width. If we want to determine the individual contributions of size and microstress, the instrumental broadening should be calibrated by using a standard material [39]. Both crystallite size and lattice strain may affect the Bragg peak in different ways. Their effects can increase the peak width, affect the peak intensity, or shift the 2θ peak position. However the peak width from crystallite size varies as $1/\cos\theta$, whereas strain varies as $\tan\theta$. The difference in behavior as a function of 2θ peak position allows one to separate the size and strain contributions on peak broadening [44]. The Williamson-Hall analysis is considered a simplified method to decouple the size-induced and strain-induced broadening by plotting the peak width as a function of 2θ, here we will use this approach to calculate the crystallite size and microstress, after the instrumental effect has been corrected by using LaB6-660a material.

5.3.2 Experiment

5.2.2.1 Sample Condition

For the sample conditions of $Pd_{0.7}Cu_{0.3}$ and pure Pd thin films, the sample conditions have the same form as that of mentioned in section 5.1.1.1.

5.2.2.2 Instrument and Parameters

For the instrumental conditions, which also have been mentioned in 5.1.1.2.

5.3.3 Results and discussion of Pd-Cu thin film

5.2.3.1 The full XRD patterns of $Pd_{0.7}Cu_{0.3}$ before and after the heat treatment

The full XRD patterns of $Pd_{0.7}Cu_{0.3}$ before and after the heat treatment are given as

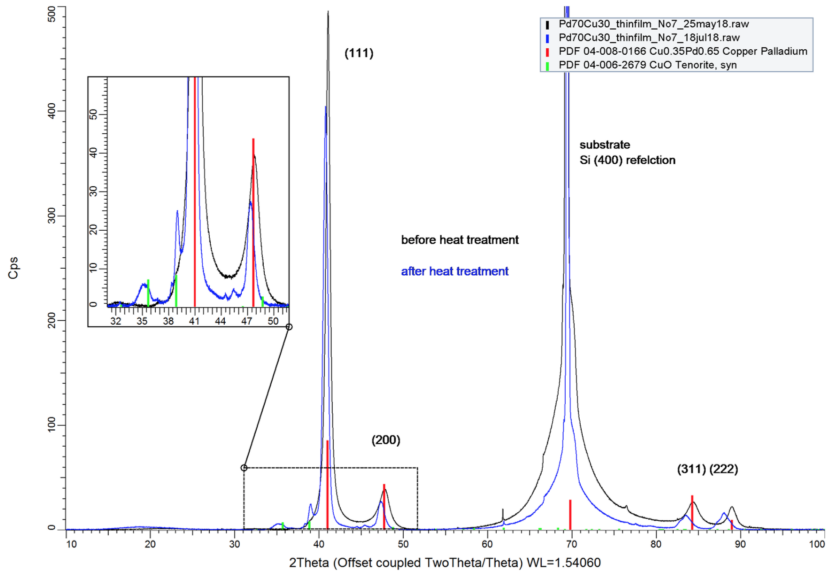

FIGURE 5.12: The full XRD patterns of unannealed and annealed $Pd_{0.7}Cu_{0.3}$ thin film (Annealing temperature: 500 K)

Where, according to this figure, the peak positions and FWHMs for (111), (200), (311) and (222) peaks will be recorded.

Furthermore, in order to separate the contributions from size and microstress in peak broadening, it is necessary to collect a XRD pattern of a standard material to determine the instrumental broadening. In this experiment, LaB_6-660a is chosen and its peak widths were measured at room temperature under the same condition as the sample thin films, where the peak positions and FWHMs (full widths at half maximum) will be recorded for all the measurable peaks. Later, the measured FWHM values of standard material will be quadratically subtracted from the sample's peak widths, thus after the instrumental correction, the FWHMs of Pd-Cu thin film will be given as

$$B = (B^2_{measured} - B^2_{instrument})^{1/2} \tag{5.31}$$

The numerical values of corrected FWHMs of $Pd_{0.7}Cu_{0.3}$ can be given as

Diffraction plane	Peak position ($2\theta^{\circ}$)	Corrected FWHM (in radian)	$Bcos\theta$	E_{hkl}	$4sin\theta/E_{hkl}$
111	41.061	0.00937	0.00877	0.19	7.38
200	47.768	0.02264	0.02070	0.073	22.19
311	84.307	0.02379	0.01764	0.103	26.06
222	88.914	0.01518	0.01084	0.19	14.74

TABLE 5.8: The corrected FWHMs of Pd-Cu thin film before the heat treatment

Diffraction plane	Peak position ($2\theta^{\circ}$)	Corrected FWHM (in radian)	$Bcos\theta$	E_{hkl}	$4sin\theta/E_{hkl}$
111	40.76443	0.01035	0.00970	0.19	7.33
200	47.34241	0.01405	0.012876	0.073	22.0
311	83.46915	0.02341	0.01747	0.103	25.85
222	87.98151	0.01908	0.01373	0.19	14.62

TABLE 5.9: The corrected FWHMs of Pd-Cu thin film after heat treatment

5.2.3.2 The measured crystallite size and microstress of Pd-Cu thin film at room temperature

The Williamson-Hall method can be effectively used to decouple the broadening of diffraction peaks that contributed from the crystallite size and microstrain [45]. Williamson and his colleagues suggested the size and strain broadening can be easily separated by plotting the peak width as a function of diffracting angle 2θ and the mathematical expression is given as

$$B = \frac{k\lambda}{Dcos\theta} + 4\epsilon tan\theta \tag{5.32}$$

By rearranging the above equation

$$Bcos\theta = \frac{k\lambda}{D} + 4\epsilon sin\theta \tag{5.33}$$

Where, D indicates the volume weighted crystallite size; k indicates a dimensionless shape factor, in this case, it is taken as 0.9, which suggests the shape of crystallite is sphere; λ indicates the wavelength of the Cu Kα_1 radiation; θ is the Bragg angle (in degrees); and B is the line broadening at half the maximum intensity, FWHM (in radians). The first term in above equation is attributed to the size-introduced line broadening, whereas the second term can be attributed to microstrain that arise from the crystal imperfection and distortion. In this method, the strain was assumed to be uniform in all crystallographic directions that considering the isotropic nature of the crystal, and all the material properties do not depend on the direction that we observe. However, the assumption of homogeneous and isotropic nature could be invalid for many anisotropic materials including Pd and Pd-based alloys. Therefore if we continue to use Eq.5.33 to determine the crystallite size and microstress, the calculated results may show a large derivation to the real situation, which are not reliable. Thus, a so-called "USDM" modified William-Hall method is introduced, where it assumes the crystals are of an anisotropic nature [39]. In this model, if we assume the microstrains that being presented in sample are small, then the Hook's law can be used to associate the strain with stress by the Young's modulus. Thus the strain ϵ (indicated in Eq.5.33) will be replaced by $\frac{\sigma}{E_{hkl}}$, where E_{hkl} is the Young's modulus in the direction perpendicular to the (hkl) planes. As a result, the above equation will be modified as

$$Bcos\theta = \frac{k\lambda}{D} + \frac{4\sigma sin\theta}{E_{hkl}} \tag{5.34}$$

Therefore, from the above equation, the modified Williamson-Hall plot can be made, with the $\frac{4sin\theta}{E_{hkl}}$ term in x-direction, and the Bcosθ term in y-direction. The the microstress will be determined from the slope of this plot, and the crystallite size will be determined from the intercept of fitting curve. The expressions of crystallite size and microstress are given as follows

$$D = \frac{k\lambda}{intercept} \tag{5.35}$$

$$\sigma = slope \tag{5.36}$$

Based on the theoretical discussion above, in our data analysis process, by using the corrected FWHMs (after instrumental calibration) and 2θ peak positions that from the XRD patterns, which measured before and after the heat treatment (provided in TABLE 5.6 and 5.7), we can plot Bcosθ as a function of $4sin\theta/E_{hkl}$, and the plot is only drawn for the preferred orientation peaks of Pd-Cu thin film, including (111), (200), (311) and (222). From the linear fit to the data, the crystallite sizes and stresses can be extracted. The Williamson-Hall plot of sample before and after heat treatment is given as

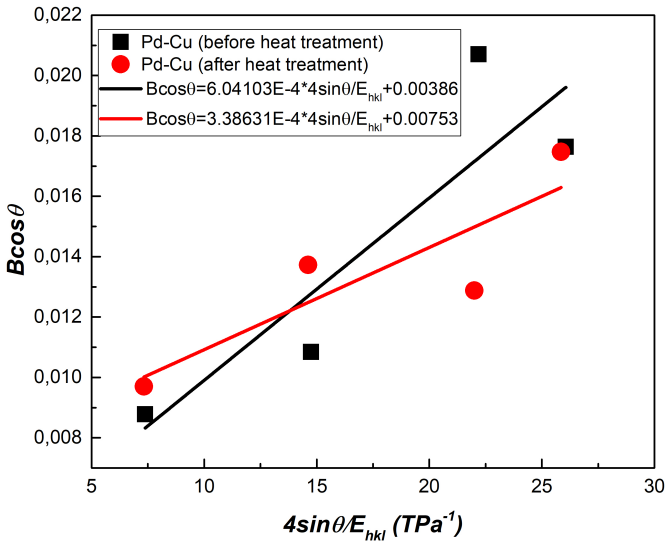

FIGURE 5.13: The Williamson-Hall plots of Pd-Cu thin film before and after the heat treatment

Where, the blue fit line represents the data measured before the heat treatment, whereas the red line represents that measured after the heat treatment; 2θs are corresponding to the peak positions of sample's various diffraction planes; and the elastic constants E_{hkl} are chosen differently relying on the various peaks, such as E_{hlk}=0.19 TPa for (111) and (222) planes, E_{hkl}=0.073 TPa for (200), and E_{hkl}=0.103 TPa for (311) planes (The derivation of E_{hkl} for different (hkl) planes will be denoted in the appendix).

However, according to the above figure, we found the derivations between the data points and the fitted line are large. Especially for (111) and (222) planes that have the

same elastic proportional constants E_{hkl}, and belong to the same type of grains, however the two points do not fit properly with the trend line. These effects may suggest the USDM Williamson-Hall method may be not precise enough for determining the crystallite size and microstress. The reasons behind would be: (1) the proportionality constants E_{hkl} of different (hkl) planes are completely independent with each other, but in many cases, the assumption may not be fulfilled; (2) the various types of grains in Pd-cu system are included in this method, however it may not be inappropriate to consider the average contributions of all grains to the peak broadening; (4) the stresses that exert on various diffraction planes are different, which may also affect the calculation results. Thus, based on these reasons, we will limit the modified Williamson-Hall method within one type of grains that have the same E_{hkl} values, in this case, only the (111) and (222) two diffraction planes will be considered. Then the modified Williamson-Hall plots of $Pd_{0.7}Cu_{0.3}$ before and after the heat treatment will be given as

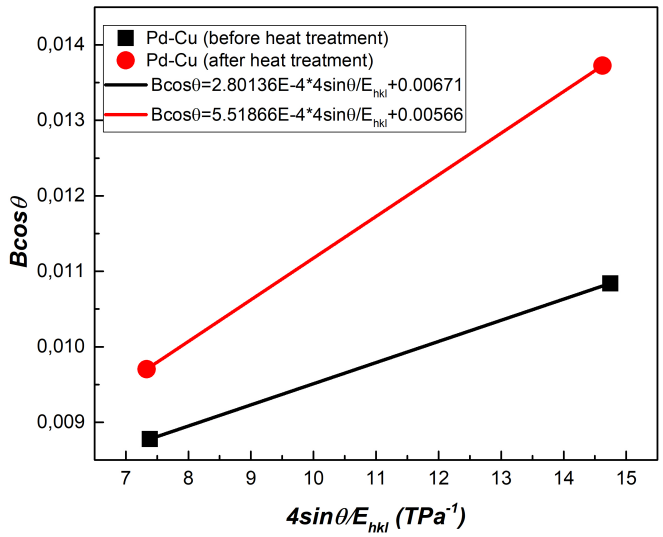

FIGURE 5.14: The Williamson-Hall plots of Pd-Cu thin film before and after the heat treatment (only the (111) and (222) diffraction planes are taken into account

Where, according to the plot, the crystallite size and the microstress can be derived via Eq.1.35 and Eq.36 separately. The calculated results are given as

Pd-Cu	Crystalline size (nm)	Microstress (MPa)
Before the heat treatment	21	280
After the heat treatment	24	552

TABLE 5.10: The calculated crystallite sizes and microstress of Pd-Cu before and after the heat treatment

Where, according to the calculation, we find the crystallite size of $Pd_{0.7}Cu_{0.3}$ alloy only grows a little bit after the heat treatment at 500 K. Moreover, the microstress also increases, which could be attributed to the segregation of Cu atoms.

5.2.3.3 The XRD high temperature measurements of Pd-Cu thin film

During the annealing procedure, in order to study the dynamic variations of the crystallite size of Pd-Cu thin film sample at 500 K, high temperature measurements were performed. However, only the (111) and (200) two peaks are considered, this is because the intensities of other peaks are too weak to be measured. For every 2 hours and 46 minutes of time interval, each scan will be completed, and the total annealing time will be longer than 60 hours, about 23 times of scans are fully completed. Here, we will not use the modified Williamson-Hall approach to do the analysis. Because the anisotropic properties of Pd-Cu, and the elastic constants E_{hkl} of (111) and (200) planes are different, which belong to the different grains, thus will only plot the variation of FWHM of individual peak with respect to the change of annealing time, to investigate the change in peak broadening that affected by the annealing time.

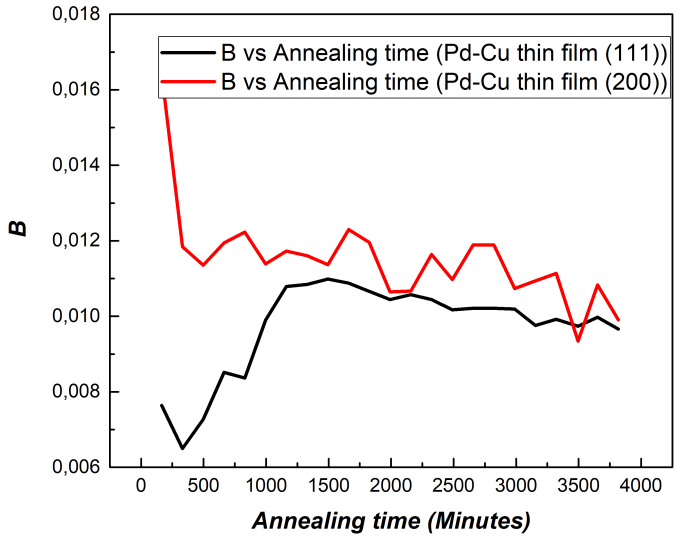

FIGURE 5.15: The dynamic changes of FWHMs for (111) and (200) peaks of Pd-Cu thin film at 500 K

Where, according to the figure, we find the the FWHM of (111) peak increases during the initial time period, later it gradually decreases with the increasing of the annealing time, and seems to fluctuate around a constant value. As for the (200) peak, its FWHM decreases sharply during the initial time, later the reduction becomes slow, which suggests the Pd-Cu thin film may approach a equilibrium state.

5.3.4 Results and discussion of pure Pd thin film

5.2.4.1 The full XRD patterns of pure Pd before and after the heat treatment

Based on the XRD analysis, the full XRD patterns of unannealed and annealed pure Pd are given in the following figure

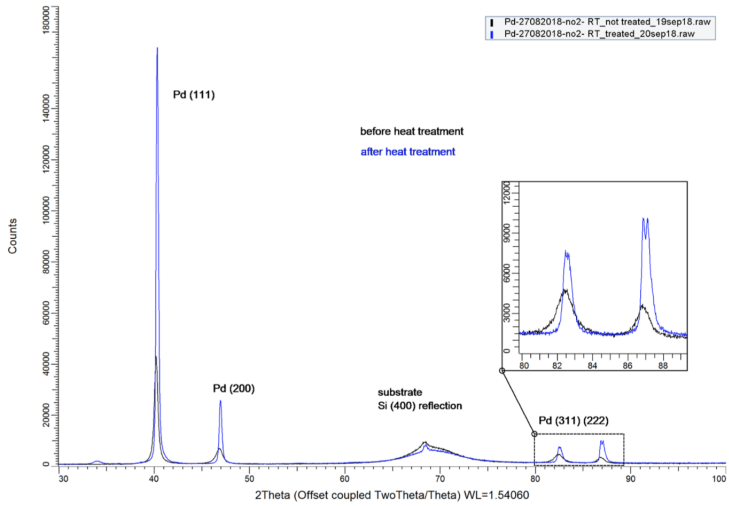

FIGURE 5.16: XRD pattern of unannealed and annealed Pd thin film (Annealing temperature: 500 K)

Where, based on this figure, the peak positions, and FWHMs will be recorded for (111), (200), (311) and (222) four diffraction planes.
The numerical values of corrected FWHMs of pure Pd can be given as

Diffraction plane	Peak position ($2\theta^{\circ}$)	Corrected FWHM (in radian)	$B cos\theta$	E_{hkl}	$4sin\theta/E_{hkl}$
111	40.1764	0.00662	0.00622	0.19	7.23
200	46.8052	0.01214	0.01114	0.073	21.76
311	82.3847	0.01558	0.01173	0.103	25.58
222	86.7881	0.00999	0.00726	0.19	14.46

TABLE 5.11: The corrected FWHMs of Pd thin film before the heat treatment

Diffraction plane	Peak position ($2\theta^{\circ}$)	Corrected FWHM (in radian)	$B cos\theta$	E_{hkl}	$4sin\theta/E_{hkl}$
111	40.2967	0.00363	0.00341	0.19	7.25
200	46.9237	0.00427	0.00392	0.073	21.82
311	82.4702	0.00630	0.00473	0.103	25.60
222	86.886	0.00625	0.00454	0.19	14.48

TABLE 5.12: The corrected FWHMs of Pd thin film after heat treatment

5.2.4.2 The measured crystallite size and microstress of pure Pd thin film at room temperature

Again, the modified Williamson-Hall method will be used to decouple the broadening of diffraction peaks that contributed from the crystallite size and microstrain of pure Pd, but only the (111) and (222) diffraction planes are taken into consideration, the reasons have already been discussed in the previous section. Then the modified Williamson-Hall plots of pure Pd are given as

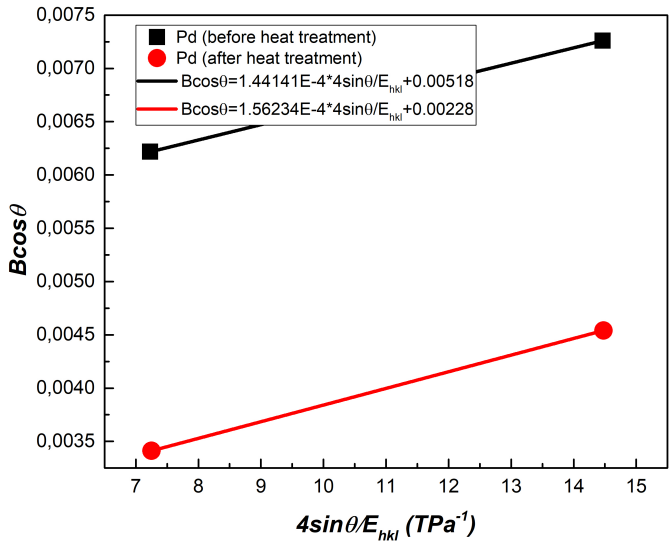

FIGURE 5.17: The Williamson-Hall plots of Pd thin film before and after the heat treatment (only the (111) and (222) diffraction planes are taken into account

Where, based on the intercept and slope of this plot, we can determine the crystallite size and microstress of pure Pd thin film, which are given as

Pd	Crystalline size (nm)	Microstress (MPa)
Before the heat treatment	27	144
After the heat treatment	61	156

TABLE 5.13: The calculated crystallite size and microstresses of Pd before and after the heat treatment

Where, based on the calculation, we find the pure Pd thin film shows a significant grain growth after the heat treatment at 500 K, and the growing degree is very large, which may suggest the segregation of solutes Cu can effectively inhibited the grain growth of pure Pd. Whereas, the calculated microstresses that measured before and after the heat treatment are close to each, which suggest the microstress that introduced by solute segregation would be large.
In this section, XRD technique is used to analyze the crystallite size and microstress by employing the Williamson-Hall method. Both the crystallite size and microstress were reported to decrease after the heat treatment, which could be attributed to the segregation, rearrangement of lattice structure or the formation of second phases, therefore further experimental examinations are required.

5.2.4.3 The XRD high temperature measurements of Pd thin film

For the analysis of the high temperature measurements that performed on (111) and (200) peaks of Pd thin film, we will plot the variation of FWHM of individual peak with respect to the change of annealing time, to investigate the change in peak broadening that affected by the annealing time.

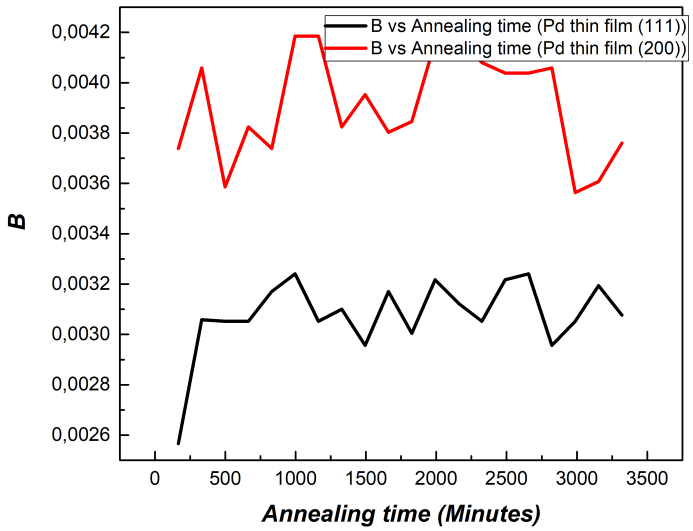

FIGURE 5.18: The dynamic changes of FWHMs for (111) and (200) peaks of Pd thin film at 500 K

Where, according to this figure, we find the FWHM of (111) peak seems to fluctuate around a constant value, which suggests the grains with the same (111) texture may arrive the stable state. Whereas for the (200) peak, the FWHMs of it is much higher than that of (111) peak, and shows a large scattering.

5.4 Conclusion of XRD analysis of Pd-Cu and pure Pd thin films

Compared the experimental results of $Pd_{0.7}Cu_{0.3}$ with that of pure Pd, we find the shift of (220) diffraction peak in Pd-cu system can be attributed to the combined influences of the solute segregation and the remained residual stresses. The change in lattice parameters of sample Pd-Cu is contributed from the change in alloy compositions, where the Vegard's law is utilized for solving the solute or solvent concentration. Based on the measurements, we find the solute concentration of Pd-Cu of bulk interior has changed from 25% into 13%, the reduction of Cu concentration in bulk interior reflect the segregation of Cu. Moreover, for Pd-Cu thin film, the measured residual stress has increased after the annealing procedure, which could be attributed to the influences of solutes segregation and the influences of thermal stresses that introduced during the thermal heating. As for pure Pd, the measured residual stress has decreased after the heat treatment, which may suggest the part of stresses are relieved during the heating procedure. In addition, according to the X-ray peak broadening analysis, both Pd-Cu and Pd samples show the grain growth phenomena, however, the degree of grain growth of Pd-Cu is much lower than that of pure Pd, which may suggest the solute (Cu) segregation can effectively reduce the grain growth to some extent.

Chapter 6

Conclusions and Recommendation

6.1 Conclusions

In this thesis, a thermodynamic grain boundary segregation model has been built, which can be used to predict the alloys' solute segregation tendency and the thermodynamic grain size stabilization.

The grain boundary segregation model is applicable for the alloys that exhibit both the strong and weak segregation tendencies with limiting ourselves to the dilute limit. Moreover, this model is also suitable for the case when rain boundary regions are considered the solid solution, the amorphous phase, or the partial solid solution and the partial amorphous phase. In this model, the Miedema model is employed for the predicting the alloy's formation enthalpy, and the ASD factor is introduced to increase the precision of the formation enthalpy that predicted by Miedema model. Some other additional energy terms are also incorporated, including the elastic strain energy (which depends on the variation of the solute concentration), fusion enthalpy (that describing the enthalpy of amorphous phase).

In order to verify the predictability of this model, several types of different metallic alloys are investigated, including the Pd-Cu, Pd-Ag, Pd-Zr, Pd-Y, Pd-Fe, Fe-Zr, Ti-Cu, Y-Fe, Ni-W and Nb-Cu binary alloys. They are examined under the same initial condition (at T=800 K, $c_0 = 0.3$), based on the calculation results, we find the solutes Cu (in Pd-Cu), Ag (in Pd-Ag), Zr (in Pd-Zr and in Fe-Zr), Y (in Pd-Y), Fe (in Y-Fe), W (in Ni-W) and Cu (in Nb-Cu) show the segregation tendency the GB region. Among them, the Pd-Zr, Pd-Y, Fe-Zr, Y-Fe, Ni-W and Nb-Cu alloys will show the strong segregation tendencies, and the calculated effective grain boundary energies are obviously decreased, but still larger than 0 ($\gamma_{gb} = 0$, implying the alloy will reach the thermodynamic equilibrium state), thus we may deduce the grain growth can not be completely inhibited. For Pd-Fe alloy, almost no segregation is predicated at 800 K. However, if we reduce the annealing temperature to 400 K or 500 K, then the Fe will segregate the GB region.

When compared the modeling results with those reported in literature, we find the model can successfully predict the grain boundary segregation of solute atoms Cu in Pd-Cu alloy, the GB segregation of Ag in Pd-Ag, the GB segregation of Zr in Pd-Zr alloy, the GB segregation of Y in Pd-Y alloy, the GB segregation of Fe in Pd-Fe alloy at a lower annealing temperature, the grain boundary segregation of Zr in Fe-Zr alloy, the grain boundary energy segregation of Fe in Y-Fe, the grain boundary segregation of W in Ni-W, the grain boundary segregation of Cu in Nb-Cu and the GB segregation of Cu in Ti-Cu at a lower annealing temperature. Therefore, we can

conclude the grain boundary segregation model could successfully predict the segregation tendency of certain alloys, and the results are comparable to those mentioned in the literature. However, the ability of predicting the alloy's grain size stability is relatively poor, this could be attributed to our simplified assumption that we neglect the influence of intermetallic or secondary phase, and only consider a single phase.

In the second part of the thesis, we introduce the X-ray diffraction analysis that performed on both $Pd_{0.7}Cu_{0.3}$ and pure Pd thin films, which includes the XRD residual stress measurement and the X-ray peak broadening analysis. For Pd-Cu binary alloy, after the heat treatment procedure (annealing condition: at 500 K for over 60 hours), we find the changes in the lattice parameter of sample Pd-Cu, which can attributed to the solute (Cu) segregation away from the bulk region. Whereas for the sample pure Pd, the lattice parameter is not affected during the heat treatment. These experimental results meet with the our modelling results. Furthermore, according to the X-ray peak broadening analysis, both Pd-Cu and pure Pd thin films experience the grain growth at 500 K , however the grain size stability of pure Pd is much poorer than the stability of $Pd_{0.7}Cu_{0.3}$, which implies the segregation of Cu indeed can stabilize the nanocrystalline material. And our modelling results indicate the grain growth of Pd-Cu can only be slightly inhibited. Moreover, the formation of PdO and CuO is observed, which suggests the experiment is not operated under the absolute vacuum condition, and the remained oxygen could become a driving force for the segregation of Cu.

6.2 Recommendation

6.2.1 Recommendation for the grain boundary segregation model

In the grain boundary segregation model, we have made several assumptions to simplify the calculations, which include: (1) we will neglect the formation of the secondary or intermetallic phases, and only the single phase will be considered, however, this is not always the case in practical applications. (2) we only consider the nearest-neighbour pairwise interactions, however, in order to have a more precise estimation result, the higher order atomic interactions should be included. Moreover, in this model, the Miedema model is employed for evaluating the formation enthalpy. However, according to the reference report [24], some statistical deviations are observed when compared the results that obtained from Miedema model with that of experimental data, and 90% of calculated results are reported to be more negative than that of experimental data. Therefore, based on these reasons, other types of simulation models are recommended, i.e., by using the Guttmann model, Kuma model and so on.

6.2.2 Recommendation for experiment

In our experimental, only the $Pd_{0.7}Cu_{0.3}$ thin film is considered. Therefore, in further investigations, the different types of alloys are suggested, i.e., Pd-Pt, Pd-Ti, etc that are lack of reference reports. Moreover, we can choose a different initial solute concentration rather than 30 wt%, select a different annealing temperature. Moreover, the oxygen should be completely evacuated in the further experiments, in order to

reduce the influences of the formed oxide on alloy's thermal stability.

In the XRD peak broadening analysis, another so called "UDEDM" modified William-Hall method is suggested, in order to decouple the influences of crystallite size and the microstress that contribute to the peak broadening. This method assumes that all the constants of proportionality E_{hkl} of different planes are no longer independent with each other [39], whereas for the "USDM" method that we used in this thesis, the E_{hkl} of different diffraction planes are completely independent with each other.

Furthermore, the crystalline sizes that estimated by using XRD technique could be inaccurate when the grain growth occurs, or when sample is annealed at high temperature [36]. Thus, in order to obtain the more accurate crystallite size, other techniques are recommended, i.e., TEM and FIB-CCI, where the grain size and the grain boundary thickness can be determined, as well as the the sample's internal sturcture, thus we can determine whether the second phases are formed after annealing.

Appendix A

Appendix A The instrumental broadening of LaB6-660a

The peak broadening can be contributed from the influences of the nanocrystallite size, the micrsotress and the instrument. The instrumental broadening will be decoupled by using a standard material. In our X-ray diffraction analysis, the $LaB_6 - 660a$ material is employed.

The XRD pattern of this standard material is given as

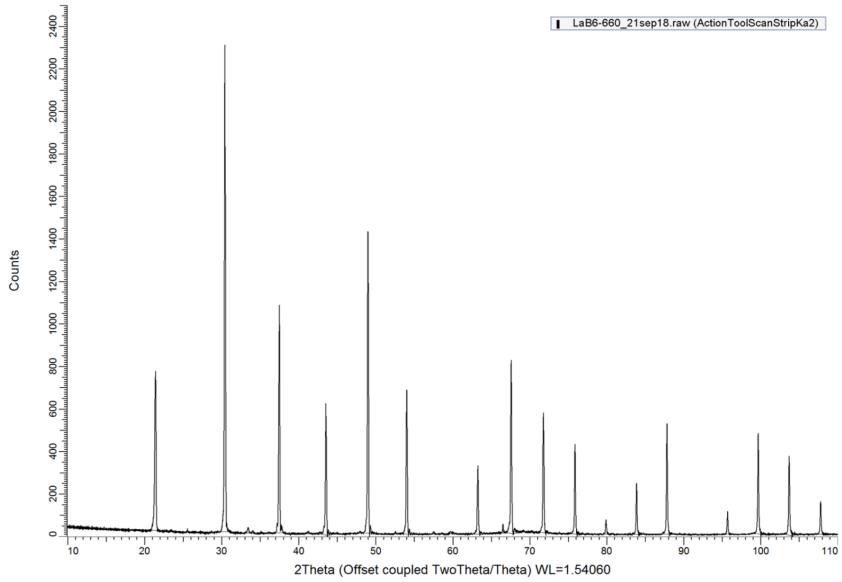

FIGURE A.1: The full XRD pattern of LaB6-660a

Where, this figure shows the LaB6-660a diffraction pattern of which the peak widths are used to determine the instrumental contributions.

For this standard material, we can plot the FWHMs of various diffraction peaks with respect to the 2θ peak postions, which gives the following form

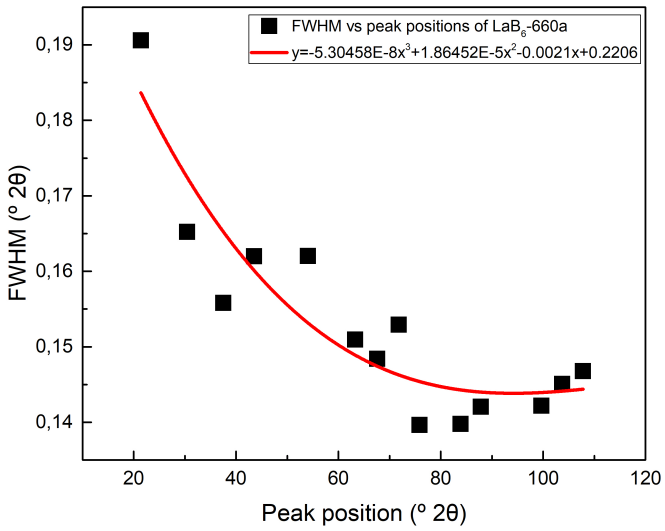

FIGURE A.2: The FWHM vs peak position for the LaB6-660a

Where, according to this figure, the instrumental broadening can be determined, then the corrected FWHMs can be determined, which is only attributed to the influences of grain size and the microstress.

Appendix B

Appendix B The calculation of E_{hkl}

The Young's modulus for a specific crystallographic plane can be given by

$$\frac{1}{E_{hkl}} = S_{11} - 2[(S_{11} - S_{12}) - \frac{1}{2}S_{44}](\alpha^2\beta^2 + \alpha^2\gamma^2 + \beta^2\gamma^2) \tag{B.1}$$

Where, S_{ij} are components of the compliance tensor, α, β, and γ are the direction cosines of the [hkl] direction and the [100], [010], and [100] direction, respectively.